JOURNAL OF COMPUTATIONAL PHYSICS 99, 1–27 (1992)

Simulation of Rollup and Mixing in Rayleigh-Taylor Flow Using the Transport-Element Method

ANANTHA KRISHNAN AND AHMED F. GHONIEM

Department of Mechanical Engineering, Massachusetts Institute of Technology, Cambridge, Massachusetts 02139

Received September 7, 1989; revised January 14, 1991

The vortex method is extended to obtain solutions of the variable density vorticity transport equation in cases when vorticity is generated by the action of gravitational body forces as well as inertial baroclinic effects. The convection of a scalar, in this case density, is simulated using the transport-element method. Similar to the vortex method, this is a grid-free, Lagrangian field method in which scalar gradients are transported along particle trajectories while being modified according to the distortion of the flow map. Results are obtained for a Rayleigh–Taylor flow evolving by the action of gravity on a finite temperature gradient. The numerical solution is validated by comparing the growth rate of small perturbations to the results of the linear stability analysis of this flow. Numerical solutions within the nonlinear range are analyzed to study the effect of density ratio on the rollup of the voriticity layer and the mixing which follows this process. © 1992 Academic Press, Inc.

I. INTRODUCTION

In this article we study the evolution of the Rayleigh–Taylor instability of a finite-thickness fluid layer across which a smooth, monotonic temperature distribution exists between a hot gas on the lower side and a cold gas on the upper side. This layer is formed by molecular diffusion which acts to smooth out a temperature discontinuity between the two gases. We will neglect the effect of molecular diffusion during the evolution of the instability assuming that convective time scales are much smaller than diffusive time scales. The gas flow is assumed to be at low Mach number and compressibility effects associated with the propagation of sound waves are neglected; i.e., the flow is incompressible with finite density gradients. We will concentrate on two-dimensional solutions during the early and late stages of the instability.

At the early stages, there is no shear or potential velocity present and the flow is driven by gravity. Kinematically, this is equivalent to saying that buoyancy drives the flow and that the vorticity production at the initial stages is due to barostatic effects. The cases considered here have high temperature ratios across the layer, from two to nine, and hence non-Boussinesq effects are important. In particular, vorticity generation due to the baroclinic torque, which evolves as material elements accelerate in a variable density field, becomes important. We will show that the redistribution of vorticity by the baroclinic torque at the later stages of development plays an important role in the mixing between the two streams.

For the purpose of simulating these density-stratified flows, we developed the transport-element method [1]. In this method, vorticity generation due to baroclinic effects associated with the interaction between density gradients and pressure gradients is retained in the formulation. The evolution of density gradients is computed using the transport-element method in which particles are employed to convect the scalar gradients along with voriticity [2, 3]. In this article, we develop a conservative version of this method suitable for the problem under discussion. Both methods can be generalized to study different forms of shear flow in two and three dimensions [4–7].

Using density discontinuity to model this flow has been suggested by many investigators to analyze the early stages of development of the flow. The same model has been successfully implemented in elaborate numerical studies using vortex representation to study the nonlinear development of this flow. For a comprehensive review and recent developments we refer the reader to Refs. [8–10]. In this work, we focus on situations where the zone of density variation has a finite thickness in the vertical direction. We also develop the linear analysis of the same flow to check the numerical solution during the early stages of the flow.

The article is organized as follows. In Section II, the formulation of the physical model is reviewed. In Section III, the extension of the vortex method to density-stratified flow is described and formulation of the transport-element method for the convection of passive scalar is presented. In Section IV, solutions of the Rayleigh–Taylor flow generated by the action of gravity on a finite temperature gradient in an unstably stratified flow are analyzed in detail. Conclusions are presented in Section V.

0021-9991/92 $3.00
Copyright © 1992 by Academic Press, Inc.
All rights of reproduction in any form reserved.

II. FORMULATION

II.1. *Governing Equations*

The nondimensional form of the governing equations for an unsteady, two-dimensional, nondiffusive gas flow are:

$$\rho T = \text{const.} \tag{1}$$

$$\mathbf{u} = \mathbf{u}_\omega + \mathbf{u}_\mathbf{p} \tag{2}$$

$$\nabla^2 \psi = -\omega; \qquad \mathbf{u}_\omega = \nabla \times \boldsymbol{\psi} \tag{3}$$

$$\nabla^2 \phi_\mathbf{p} = 0; \qquad \mathbf{u}_\mathbf{p} = \nabla \phi_\mathbf{p} \tag{4}$$

$$\frac{d\omega}{dt} = \frac{1}{\rho^2} (\nabla \rho \times \nabla p) \tag{5}$$

$$\frac{dT}{dt} = 0. \tag{6}$$

We assume that the flow is at low Mach number. The assumption of low Mach number flow states that the velocity of sound is much larger (infinite in the limit) than that of the flow and hence the pressure is equalized instantly across the flowfield. Therefore, spatial pressure variations due to the acceleration of the fluid are small in comparison to the total pressure and hence do not affect the local density of the fluid. Under these conditions, the pressure term in the state equation is a function of time only and not of space. If the flow is in an infinite domain, the pressure can be assumed to be independent of time and the product of density and temperature, for a perfect gas, reduces to a constant as in Eq. (1). Moreover, the pressure term in the energy equation is neglected in comparison to the other terms as in Eq. (6). Although the low Mach number assumption is used to decouple the density from spatial pressure variations, the pressure term is still retained in the equation of motion to balance the momentum changes in the flowfield as shown in Eq. (5). This is because, in the momentum equation, the pressure term is of the same order of magnitude as the fluid acceleration. The fluids in both streams are assumed to behave as perfect gases with equal molecular weights and constant specific heats. The Reynolds number is high and hence the effect of viscosity and molecular diffusion are neglected beyond $t = 0$. For the details of the derivation of Eqs. (1)–(6), see [11–13].

The definitions of the symbols are as follows: $d/dt = \partial/\partial t + \mathbf{u} \cdot \nabla$ is the Lagrangian derivative along a particle trajectory, t is time, ρ is the local fluid density, $\mathbf{u} = (u, v)$ is the fluid velocity, $\mathbf{x} = (x, y)$ is the space coordinate, x and y being the horizontal and vertical directions, respectively, ϕ is a velocity potential, $\boldsymbol{\psi} = \psi \mathbf{e}_z$ is a streamfunction defined such that $\mathbf{u}_\omega = \nabla \mathbf{x} \boldsymbol{\psi}$, where $\boldsymbol{\omega} = \nabla \mathbf{x} \mathbf{u}$ is the vorticity, $\mathbf{e}_z$ is the unit vector normal to the x-y plane, and $\mathbf{u}_p$ is a potential velocity, $\nabla \cdot \mathbf{u}_p = 0$, added to satisfy the normal velocity boundary conditions across the boundaries of the domain. ∇ and ∇^2 are the gradient and the Laplacian operators, respectively. Variables are nondimensionalized with respect to an appropriate combination of a characteristic density ρ_0, velocity U_0, and length L_0. For the Rayleigh–Taylor flow we use the parameters $\rho_0 = \rho_h$ the (higher) density of the top stream, $u_0 = \sqrt{L_0 gr}$, where $L_0 = \sqrt{2}\, S$ and S is the characteristic thickness of the initial density distribution and gr is the gravitational acceleration, and $p_0 = \rho_0 U_0^2$ for the pressure.

Equation (5) is derived by taking the curl of the momentum equation:

$$\frac{du}{dt} = -\nabla p/\rho - j \tag{7a}$$

where j is the unit vector in the vertical y-direction. We also note that Eq. (7a) can be rewritten as

$$\nabla p = -\rho \left(\frac{du}{dt} + j \right) \tag{7b}$$

which explicitly relates the pressure gradient to the material and gravitational acceleration. Furthermore, Eqs. (1) and (6) can be combined to show that

$$\frac{d\rho}{dt} = 0, \tag{8}$$

indicating that the density is constant along the material particle trajectory, $\rho(\chi(\mathbf{X}, t) = \rho(\mathbf{X}, 0)$, where $\chi(\mathbf{X}, t)$ is the coordinate of the particle starting at $x = \mathbf{X}$ at $t = 0$.

III. NUMERICAL SCHEMES

III.1. *The Vortex Method for a Variable-Density Flow*

The vortex method is used to solve the vorticity transport equation. We start by deriving an expression for the velocity distribution induced by a given vorticity field. If the domain is unbounded then the solution of Eq. (3) can be written as

$$\psi(\mathbf{x}) = \int G(\mathbf{x} - \mathbf{x}')\, \omega(\mathbf{x}')\, d\mathbf{x}', \tag{9}$$

where G is the Green's function of the Poisson equation. In two dimensions, $G = -1/2\pi\ (\ln r)$, where $r^2 = x^2 + y^2$. The vortical component of the velocity is the curl of the streamfunction,

$$\mathbf{u}_\omega(\mathbf{x}) = \int \mathbf{K}(\mathbf{x} - \mathbf{x}')\, \omega(\mathbf{x}')\, d\mathbf{x}', \tag{10}$$

where $\mathbf{K} = -1/2\pi r^2(-y, x)$ is the kernel of the Poisson equation. Equations (5) and (10) form the basis of the vortex method. At each time step, the vortical component

obtained from Eq. (10) is complemented with the potential velocity, constructed to satisfy the normal boundary conditions, to compute the fluid velocity which is then used in Eq. (5) to update the vorticity. One advantage in representing the flow in terms of vorticity is that the region of finite vorticity is usually confined to a small part of the flowfield, especially at high Reynolds numbers, and all the computational effort can be concentrated on resolving this region rather than discretizing the equations over the entire flow domain. Thus, the numerical resolution for a given computational expense is maximized. Vortex methods are Lagrangian methods wherein particles, which transport flow properties, are followed in time and space. Lagrangian schemes eliminate the necessity to deal with the nonlinear convective terms explicitly, i.e., spatial derivatives constituting ∇u are not required.

To improve the accuracy and extend the application of vortex methods to highly unsteady flows with large strain rates, we formulated the vortex-element method [1, 2, 5]. In this method, the vorticity is accurately discretized, using collocation methods, among finite area elements that move along particle trajectories. Each element transports a finite amount of vorticity. The distribution of vorticity associated with each element is described by a radially symmetric function, f_δ, with a characteristic radius, δ, such that most of the vorticity is concentrated within $r < \delta$, where r is the distance measured from the center of the element. Vortex elements are initially distributed over the area of the flow where $|\omega| > 0$ such that the discretization error is less than a predetermined tolerance parameter ε. Typically ε is around 10^{-5}. The strength of the vortex element is determined by collocation; for the element located at $\mathbf{X}_i$, the vorticity, denoted by ω_i, is obtained from the solution of the system of equations:

$$\boldsymbol{\omega}(\mathbf{X}, 0) = \sum_{i=1}^{N} \boldsymbol{\omega}_i h^2 f_\delta(|\mathbf{X} - \mathbf{X}_i|), \tag{11}$$

where $\omega(\mathbf{X}, 0)$ is the vorticity distribution at $t = 0$. The core function, f_δ, is chosen to be a second-order Gaussian, given by $f_\delta(r) = (1/\pi\,\delta^2)\exp(-r^2/\delta^2)$. Note that f_δ is a function of the absolute value of the distance between the element and the point. The absolute sign will be suppressed for convenience. Equation (11) is equivalent to expanding a function $\omega(\mathbf{x})$ in terms of a number, N, of kernel functions, f_δ, located at $\mathbf{X}_i$ and with weights $\Gamma_i = \omega_i h^2$, and h is the distance between the centers of neighboring elements. The accuracy of the discretization depends on the choice of the core function f_δ, the initial distribution of the particles, the method of determining the initial values of values of ω_i or Γ_i, $i = 1, 2, \ldots, N$, and the ratio δ/h. The selection of the core function for a particular accuracy was extensively discussed in Refs. [2, 14–16]. Accurate discretization and long time accuracy of the computed flowfield require that $\delta/h > 1$.

For an initially smooth distribution of vorticity, we found that $\delta/h = 1.0$–1.3 is sufficient to limit the discretization error to the desired value, ε [2]. Note that although the core function is constructed as a rapidly decaying function, such as an nth-order Gaussian, the fields of individual vortex elements are strongly overlapping due to the choice of δ/h. Thus, according to Eq. (11), the local value of the vorticity at a point is determined by the contributions of all the elements in the field. Therefore, the vorticity at any point in the flowfield at any time is determined by

$$\omega(\mathbf{x}, t) = \sum_{i=1}^{N} \Gamma_i(t) f_\delta(\mathbf{x} - \boldsymbol{\chi}_i(\mathbf{X}_i, t)), \tag{12}$$

where $\Gamma_i = \omega_i h^2$ is the total circulation of an element and is obtained as a function of time from the solution of the vorticity transport equation as will be shown next, h is the geometric average of the distance between the centers of neighboring elements in the two perpendicular directions, and $\boldsymbol{\chi}_i$ is the trajectory of the particle. The velocity field of a distribution of vortex elements is obtained by substituting Eq. (12) into Eq. (10) and integrating. The resulting expression is

$$\mathbf{u}_\omega(\mathbf{x}, t) = \sum_{i=1}^{N} \Gamma_i(t)\, \mathbf{K}_\delta(\mathbf{x} - \boldsymbol{\chi}_i(\mathbf{X}_i, t)) \tag{13}$$

and

$$\mathbf{K}_\delta(\mathbf{x}) = -\frac{(y, -x)}{2\pi r^2}\,\kappa\left(\frac{r}{\delta}\right) \tag{14}$$

$$\kappa\left(\frac{r}{\delta}\right) = 1 - \exp(-r^2/\delta^2), \tag{15}$$

where Eq. (15) is obtained for second-order Gaussian elements.

Depending on the nature of the flow domain, a potential component must be added to $\mathbf{u}_\omega$ in order to satisfy the normal velocity boundary conditions. For all the cases computed in this study, the flow is infinite in the y-direction and infinitely periodic in the x-direction with a periodicity length λ. The potential component is obtained by taking into account the velocities generated by an infinite number of images in the x-direction for each computational element in the domain. The total velocity is given as

$$\mathbf{u} = \sum_{i=1}^{N} \left[\frac{\Gamma_i}{2\pi} \left\{ \sum_{j=0}^{\pm 1} \frac{(\Delta y, -(\Delta x + j\lambda))}{((\Delta x + j\lambda)^2 + \Delta y^2)} \times \exp\left(-\frac{((\Delta x + j\lambda)^2 + \Delta y^2)}{\delta^2} \right) + \frac{\pi}{\lambda} \times \frac{(-\sinh(2\pi\,\Delta y/\lambda), \sin(2\pi\,\Delta x/\lambda))}{(\cosh(2\pi\,\Delta y/\lambda) - \cos(2\pi\,\Delta x/\lambda))} \right\} \right], \tag{16}$$

where $\Delta x = x - x_i$, $\Delta y = y - y_i$, N is the total number of computational elements in the domain $0 < x < \lambda$. Since the core function, f_δ, is a rapidly decaying function, its effect is included only for the nearest images on both sides of the domain. The above expression is used to compute the velocity at the center of each computational element in order to displace the elements along the particle path according to:

$$\frac{d\chi_i}{dt} = \mathbf{u}(\chi_i(\mathbf{X}_i, t), t). \tag{17}$$

For a barotropic, or uniform-density flow, the vorticity and circulation of each element is conserved along the particle path and is independent of time, and hence $\omega_i(t) = \omega_i(0)$.

As time progresses, the generation of strong strain with the growth of perturbations into the non-linear stage increases the distance between neighboring elements, $\delta\chi$, in the direction of maximum strain beyond the desired value of h. Thus, the accuracy of spatial discretization, which is governed by δ/h, is adversely affected. In the computations, deterioration of accuracy is observed in the generation of disorganized, random motion, on the scale of h, which grows as time progresses. To avoid this problem, more elements are introduced where $\delta\chi > \beta h$, where $\beta \sim 1.5$, and the circulation of the original two elements is locally redistributed among the newly introduced elements. Since the circulation of each element is $\omega_i h^2$ and since the vorticity is conserved along a particle path, the redistribution of circulation is accomplished by dividing the value of h^2 of the original two elements equally among the newly generated elements and the original elements. By increasing the number of vortex elements, we ensure that the underlying grid of computational elements can capture the instantaneous vorticity distribution as it evolves with the motion of the flow. The need to increase the number of elements becomes clear when realizing that as the flow develops strong strains, the streamlines become strongly convoluted and require more particles to describe their geometry accurately [3, 18].

The vorticity will remain constant along the particle path if the value of δ^2 is adjusted so that the ratio of δ^2/h^2 is maintained constant in Eq. (12). Thus, the core radius of an element is effectively decreased as the element is exposed to strong positive strain. Reducing the size of the cores of vortex elements helps minimize the numerical diffusion which may accumulate to unacceptable levels if the area on which the vorticity exists is allowed to grow beyond its original size.

The redistribution of vorticity in the direction of maximum tensile strain among more elements with smaller cores requires maintaining a list of near neighbors in the direction of maximum strain and updating this list each time step according to the changes in the vorticity distribution along the layer. This process is equivalent to utilizing a one-dimensional moving grid along each individual layer of vortex elements to preserve the organization of the computations. It is also used to provide information about the flow map at any time step since, according to the condition of incompressibility, one can compute the changes in the length of the material layers normal to the line of vortex elements by knowing the extension of the elements in the direction of maximum strain.

For a baroclinic flow, the vorticity is no longer conserved along the particle path. The interaction between the density gradient and the pressure gradient in Eq. (5) leads to the generation of baroclinic vorticity. In terms of the circulation, the change in total vorticity of a vortex element is given by

$$\frac{d\Gamma_i}{dt} = -\frac{\nabla\rho_i}{\rho_i} h_i^2 x \left(\frac{d\mathbf{u}}{dt} + j\right)_i, \tag{18}$$

where the pressure gradient in the baroclinic term is replaced by the inertial and gravitational acceleration using the momentum equation, Eq. (7b). The inertial acceleration of an element is computed by numerically differentiating its velocity between two time steps, and the local value of the density gradient and the density are computed using the transport-element method described in the next section.

The computations of vorticity transport proceed in a fractional step scheme as follows: (1) vortex elements are transported according to the velocity computed at their centers without changing the circulation or the size of individual elements; (2) the elements that experience strong strain are split (or combined if the strain is negative) and the values of the core and circulation of the original elements are distributed among the new elements; and, (3) Eq. (18) is integrated for each element according to the local acceleration, density, and density gradient to compute the new values of the element strength.

We note that, as in any fractional step scheme, one has to be careful in choosing the time step, Δt, in order to preserve accuracy. This is because a fractional step scheme, without symmetric splitting, maintains accuracy $O(\Delta t)$. Iteration may become necessary if the density ratio or the strain rate, which governs the rate of vorticity production, is large. In our calculation, however, we did not find it necessary to use iteration in any of the simulations presented below. Instead, we utilized a time step control strategy in which Δt was reduced when $\Delta\omega_i = \omega_i(t) - \omega_i(t - \Delta t)$ exceeded a given fraction of $\omega_i(t)$.

III.2. *The Transport-Element Method*

Another application in the development of particle methods to variable density flows is the formulation of the transport-element method to compute the scalar distribu-

tion in a Lagrangian form. In this scheme, the gradient of the scalar field is discretized into a number of finite area elements using Eq. (12) with ω replaced by $\mathbf{g} = \nabla s$, where s is a conserved scalar such as the temperature or density. Similar to vortex elements, the transport elements are distributed where $|g| > 0$ and are displaced along the particle path with the velocity computed at the centers of the elements. Each element transports a finite value of the scalar gradient and the value of the scalar is recovered as a summation over all the particles. The scalar gradient transported by each element is updated by integrating the gradient transport equation which is obtained by taking the gradient of the scalar transport equation. The conservation equation for a conserved scalar (such as temperature or density) can be written as

$$\frac{\partial s}{\partial t} + \mathbf{u} \cdot \nabla s = 0 \tag{19}$$

where s is the conserved scalar. The transport equation for the scalar gradient is obtained by taking the gradient of the above equation,

$$\frac{\partial \mathbf{g}}{\partial t} + \mathbf{u} \cdot \nabla \mathbf{g} + \mathbf{g} \cdot \nabla \mathbf{u} + \mathbf{g} \times \boldsymbol{\omega} = 0, \tag{20}$$

where $\mathbf{g} = \nabla s$ is the gradient of the scalar. Equation (20) is integrated for $\mathbf{g}$ as a function of time for each element. This requires the computation of the velocity gradient by analytically differentiating Eq. (16). This process can be computationally expensive if the number of elements in the field is large. Moreover, small errors in integrating Eq. (20) can lead to large errors in the scalar concentration. Another method is now proposed to compute g without integrating Eq. (20) and without the need to differentiate the velocity field. In this method, the information obtained from the flow map is used to update g. We start by rewriting Eqs. (19) and (20) along a particle path:

$$\frac{ds}{dt} = 0 \tag{21}$$

and

$$\frac{d\mathbf{g}}{dt} = -\mathbf{g} \cdot \nabla \mathbf{u} - \mathbf{g} \times \boldsymbol{\omega}. \tag{22}$$

Equations (21) and (22) show that while the scalar, s, is conserved along a particle path, its gradient, $\mathbf{g}$, changes due to the action of the strain field and local vorticity. If the material is exposed to a strong strain in the direction normal to the gradient, the value of g must increase by the same amount as the stretch in the material element. Figure 1a shows a schematic of a rectangular fluid layer with the initial scalar gradient perpendicular to the material length everywhere, the top and bottom sides of the element are isoscalar lines. Figure 1b shows the same element after it has been deformed by a flowfield similar to what is encountered in a shear layer [2]. Since the scalar is conserved, material lines which were isoscalar lines must remain as isoscalar

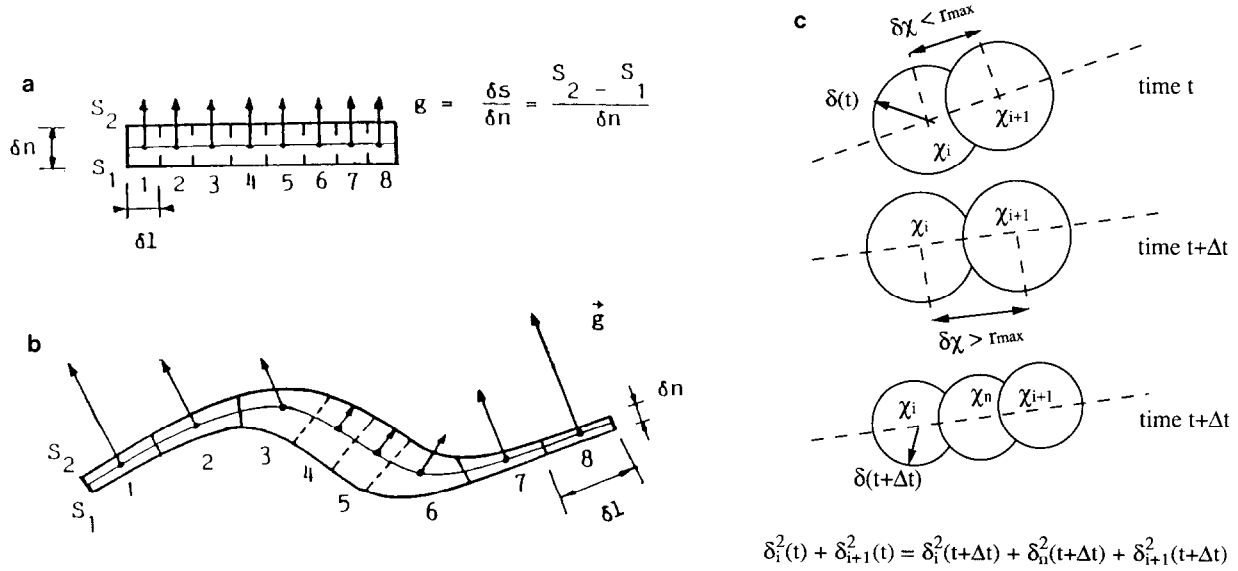

FIG. 1. (a) A material layer, of thickness δn, separating two constant scalar lines, S_1 and S_2. The layer is divided into eight transport elements, each with length δl. The gradient supported by this layer, and assigned to each element, is $g = \delta S/\delta n$. (b) The same material layer after being exposed to strain and rotation (the streamwise coordinate is expanded), showing how g changes its value and direction with strain and rotation, respectively. The deformation assumed in this illustration is of the type encountered in Kelvin–Helmholtz instability [2]. (c) The changes in the core radius of the transport elements due to the action of strain; r_{max} is the maximum allowable distance between neighboring elements.

lines, i.e., the gradient must still be perpendicular everywhere to the material lines. The magnitude and direction of g are indicated in Fig. 1b. The magnitude of the gradient increases in regions of positive strain and decreases in regions of negative strain. Also, since the material lines are rotated due to the action of the flowfield, the direction of the gradient is rotated so as to maintain $\mathbf{g}$ perpendicular to the material lines. A mathematical expression relating $\mathbf{g}$ to the flowfield is now developed using the conservation equations.

The magnitude of $\mathbf{g}$ can be calculated by deriving an equation that governs $g = |\mathbf{g}|$. To do this, Eq. (22) is expanded in terms of $g\mathbf{n}$, implementing kinematical relations that describe the variations of $\mathbf{n} = \mathbf{g}/g$, the unit normal vector to the isoscalar line. After lengthy manipulations, the following expression is obtained (see Appendix I for derivation):

$$\frac{dg}{dt} = -g\mathbf{n} \cdot (\mathbf{n} \cdot \nabla \mathbf{u}). \tag{23}$$

Moreover, $\mathbf{g} = (ds/dn)\mathbf{n} \sim (\delta s/\delta n)\mathbf{n}$, where δs is the variation of s across a small material line δn. Furthermore, according to Eq. (21), a material line which is initially aligned with an isoscalar line will remain aligned with the same line. The variation of a material vector element $\delta \boldsymbol{l}$ is governed by [20]:

$$\frac{d\,\delta \boldsymbol{l}}{dt} = \delta \boldsymbol{l} \cdot \nabla \mathbf{u}, \tag{24}$$

where $\delta \boldsymbol{l} = \delta l\, \boldsymbol{l}$ and $\boldsymbol{l}$ is the unit vector along the material. A material line is also an isoscalar line, and $\boldsymbol{l}$ is perpendicular to $\mathbf{n}$. For an incompressible flow, $\nabla \cdot \mathbf{u} = 0$, it can be shown that the equation for δl is given by

$$\frac{d\,\delta l}{dt} = -\delta l(\mathbf{n} \cdot (\mathbf{n} \cdot \nabla \mathbf{u})). \tag{25}$$

The equation governing the variation of δl is the same as that of g. It follows that $g/\delta l = \text{constant}$ along a particle path. Since $g \sim \delta s/\delta n$, the constant turns out to be $\delta s/h^2$, where $h^2 = \delta l.\ \delta n$ is the material area of the fluid element. Therefore, the magnitude of $\mathbf{g}$ is proportional to the magnitude of δl and its direction is always normal to the vector $\boldsymbol{l}$. Since Lagrangian calculations involve tracking material lines and surfaces, the magnitude and direction of δl are always known. Thus $\mathbf{g}$ is completely determined as a function of time without having to integrate Eq. (22).

A general expression for the scalar gradient can be written as

$$\mathbf{g}(t) = \frac{\delta s\, \delta l(t)}{h^2(0)}\, \mathbf{n}(t), \tag{26}$$

where $h^2(0)$ is the initial area at $t = 0$ associated with the fluid element. This relation can be used to construct a scheme which is compatible with the vortex method to compute the evolution of the scalar field. The scalar gradient field is discretized among a number of elements which are transported along the particle path while the gradients vary according to Eq. (26). Thus,

$$g(\mathbf{x}, t) = \sum_{i=1}^{N} \mathbf{g}_i(t)\, h_i^2(t)\, f_\delta(\mathbf{x} - \boldsymbol{\chi}_i(\mathbf{X}_i, t)), \tag{27}$$

where $\boldsymbol{\chi}_i(\mathbf{X}_i, t)$ is, as before, the particle path. Equation (27) is based on the expansion of $\mathbf{g}$ in terms of the core functions f_δ. All the comments made before regarding the accuracy of such a representation apply to Eq. (27). Since an isoscalar line is a material line in a nondiffusive field, $\delta \boldsymbol{l}_i$ can be updated as: $\delta \boldsymbol{l}_i(t) = (\boldsymbol{\chi}_{i+1} - \boldsymbol{\chi}_{i-1})/2$, while $\mathbf{n}_i \cdot \boldsymbol{l}_i = 0$ and $\boldsymbol{l}$ is the unit vector in the direction of the isoscalar line and normal to the vector $\mathbf{n}$. Thus, it suffices to move the centers of the transport element, while remembering the near neighbors at $t = 0$ to compute the scalar flux. When an element is inserted between two neighboring elements, the values of $\delta \boldsymbol{l}_i$ are redistributed between the three elements and h^2 and δ^2 are adjusted so that the total material area is conserved. Figure 1c shows a schematic representation of this process. The gradient for each element is updated in time according to

$$\mathbf{g}_i(t) = \frac{\delta s_i \delta l_i(t)}{h_i^2(0)}\, \mathbf{n}_i(t), \tag{28}$$

where the subscript i refers to the element i.

Given the location and strength of the transport elements, the scalar concentration is computed by direct integration over the fields of the transport elements. The divergence of the vector $\mathbf{g}$ is given by $\nabla^2 s = \nabla \cdot \mathbf{g}$. In analogy to the streamfunction ψ, the solution for s in an infinite domain is given by $\mathbf{s} = \int \nabla \cdot \mathbf{g}\, G\, d\mathbf{x}$, where $G = -\frac{1}{2}\pi \ln r$ is the Greens function of the Poisson equation. Thus, the transport elements act as sources of strength equal to the divergence of the scalar flux, $\nabla \cdot \mathbf{g}$. After integration by parts, it can be shown that $s = \int \mathbf{g} \cdot \nabla G\, d\mathbf{x}$. The expression for $\mathbf{g}$, Eq. (27), is substituted into the above expression to obtain

$$s(\mathbf{x}, t) = \sum_{i=1}^{N} \mathbf{g}_i(t)\, h_i^2(t) \cdot \nabla G_\delta(\mathbf{x} - \boldsymbol{\chi}_i(\mathbf{X}_i, t)), \tag{29}$$

where

$$\nabla G_\delta(\mathbf{x}) = \frac{(x, y)}{2\pi r^2}\, \kappa\left(\frac{r}{\delta}\right), \tag{30}$$

including the effect of the images:

$$s(\mathbf{x}, t) = \sum_{i=1}^{N} \left[\frac{\mathbf{g}_i h_i^2}{2\pi} \cdot \left\{ \sum_{j=0}^{\pm 1} \frac{-((\Delta x + j\lambda), \Delta y)}{((\Delta x + j\lambda)^2 + \Delta y^2)} \times \exp\left(-\frac{((\Delta x + j\lambda)^2 + \Delta y^2)}{\delta^2} \right) + \frac{\pi}{\lambda} \times \frac{(\sin(2\pi \Delta x/\lambda), -\sinh(2\pi \Delta y/\lambda))}{(\cosh(2\pi \Delta y/\lambda) - \cos(2\pi \Delta x/\lambda))} \right\} \right]. \tag{31}$$

This formulation is fully compatible with the vortex method since all the information needed to compute the scalar transport is already a part of the vortex computations, including all the expressions for the Green functions. In actual computations, there is no need to distinguish between vortex elements and transport elements. A transport element can be used to transport either or both vorticity and scalar gradients. Once introduced, its vorticity and scalar gradients change according the appropriate expressions. The algorithm of the transport-element method proceeds as follows: (1) The velocity at the centers of the elements is calculated by summing the vortical and potential components. This velocity is used to displace the elements along the particle path. (2) The magnitude and alignment of $\delta \boldsymbol{l}_i$ is found for each element. Using this information, the new value of $\mathbf{g}$ is calculated from Eq. (28). (3) The core radii of the elements are updated according to the strain field. (4) The scalar is computed as a summation over all the elements according to Eq. (31).

IV. THE RAYLEIGH–TAYLOR INSTABILITY

IV.1. *Definition*

Rayleigh–Taylor instability develops when two fluids of different densities are stratified in a field such that the density gradient and the gravitational acceleration are not perfectly aligned. Some phenomena in which RT instability occurs include: (i) the downwash of heavier air due to a temperature gradient in the atmosphere; (ii) the rise of a hot bubble in fires and explosions; (iii) the oscillation in a buoyant jet diffusion flame. In this work, we consider a finite-thickness layer separating two fluids at different temperatures. The layer is initially formed by the diffusion of heat from the hot fluid on the bottom to the cold fluid on the top side. The layer is the zone where $\rho_h < \rho < \rho_c$, where ρ_h and ρ_c are the densities of the hot and cold fluid, respectively. For $t > 0$, we neglect diffusion, assuming that diffusive time scales are much larger than convective time scales.

IV.2. *Description of Flow Geometry*

A schematic for the flow in which the RT instability is analyzed is shown in Fig. 2. The density varies as an error function in the y-direction and the gravitational force acts in the negative y-direction. At $t = 0$, the fluid is stationary and the initial vorticity is zero. The layer between the two fluids is perturbed by a cosine wave. The flow is periodic in the x-direction with a periodicity length equal to the wavelength of the perturbation. The domain is infinite in the y-direction.

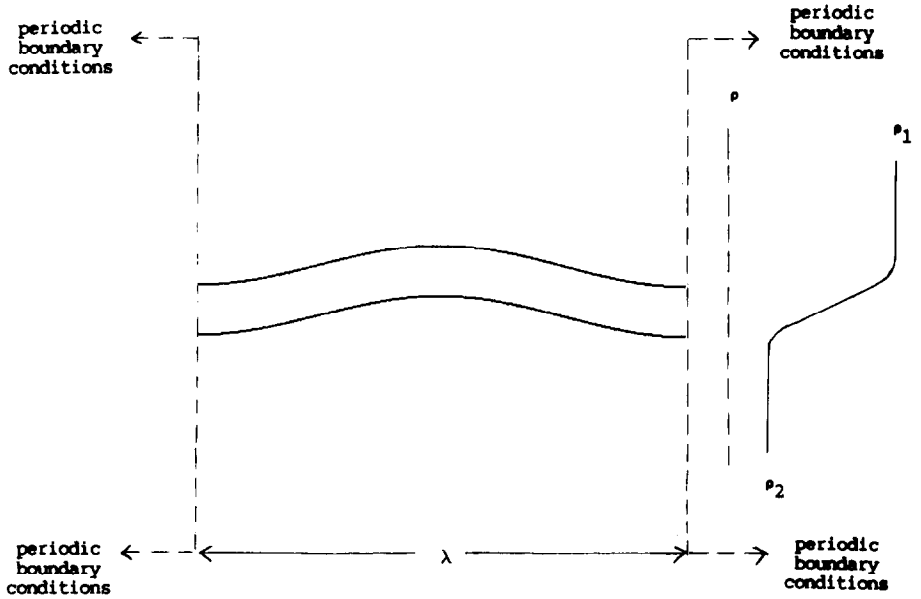

FIG. 2. A schematic of the Rayleigh–Taylor instability in a gravitational field. The density of the top fluid is higher than that of the bottom fluid. The error function distribution on the right side is the density distribution at time $t = 0$.

In all the computations reported here, we used the following numerical parameters: the density layer is divided into 15 rows in the y-direction; each row is discretized into 40 elements, i.e., $h = \sqrt{h_x h_y} = 0.28$. The core radius δ is initially taken as $\delta = 0.3$ $(= 1.07h)$. At $t = 0$, the strength of the elements are obtained by solving the linear system obtained from Eq. (11) for the vorticity and density gradients. Using this value of h/δ, the difference between the total circulation and the sum over all the elements is less than 1.E-0.5. The time step is $\Delta t = 0.1$. As the computation progressed into the nonlinear stages, Δt was reduced to control the accuracy. The ordinary differential equations describing the motion of the particles, Eq. (17), and the variation of the vorticity along the particle path, Eq. (18), are integrated using a fourth-order Runge–Kutta method with time step control. The inertial acceleration along a particle path is computed using a compatible numerical differentiation formula, i.e., a fourth-order formula based on the values of the velocity computed in the substeps of the Runge–Kutta integration. Convergence studies of the vortex element method were presented before and their results were used in the choice of the numerical parameters [2].

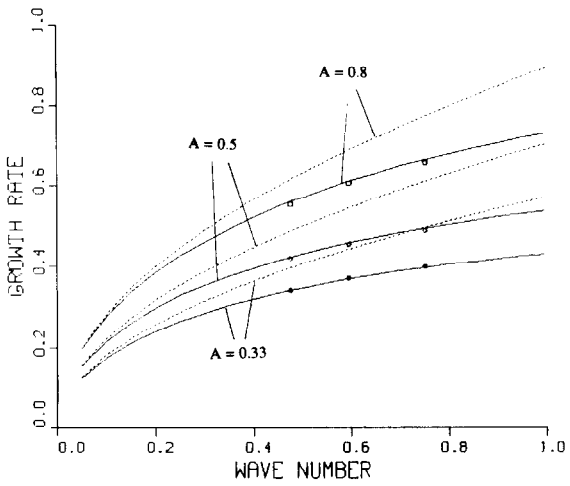

FIG. 3. The linear growth rate of the RT instability as a function of the wavenumber. The three density ratios are $r_\rho = 2$, 3, and 9, wich correspond to Atwood number $A = 0.33$, 0.5, and 0.8, respectively. Solid lines represent the results of the linear theory for a finite thickness layer and broken lines are the results of the linear theory for a zero-thickness interface. The symbols are results of numerical simulations.

IV.3. *Linear Stability Analysis*

The Rayleigh equation for the linear stability of the finite-thickness RT problem is derived in the same way as for the finite-thickness Kelvin–Helmholtz instability except that the effect of gravity is included in the equations of motion [6]. Using the fact that the initial velocity is zero everywhere in the domain, the Rayleigh equation is reduced to

$$\mathbf{v}'' = -\frac{R'}{R}\mathbf{v}' + \left(\frac{R'gr}{R\mathbf{c}^2} + \alpha^2\right)\mathbf{v} \tag{32}$$

where $\mathbf{v}$ is the vertical velocity, R is the cross-stream density distribution, gr is the gravitational acceleration, $\mathbf{c} = c_r + ic_i$. In this case, $c_r = 0$ since the initial velocity distribution is zero and, $'$ and $''$ refer to the first and second order derivatives with respect to y. For a given value of the wavenumber, the solution for $c\,(= ic_i)$ is obtained by iteration [6].

Results of the linear stability theory are shown in Fig. 3. The growth rate $(= -\alpha c_i)$, shown as solid lines, is obtained for three cases in which the density ratio $r_\rho = \rho_c/\rho_h = 2$, 3, and 9. The linear growth rate for a zero-thickness interface is given as $n = \sqrt{A\alpha}$, where $A = (\rho_c - \rho_h)/(\rho_c + \rho_h)$ is the Atwood number [17]. The corresponding Atwood numbers for the cases considered here are 0.33, 0.5, and 0.8, respectively. The growth rate is smaller for the finite-thickness layer than for the infinitely thin layer. The reason for the reduction in the growth rate as the thickness of the density layer increases is as follows. In the first case, vorticity is generated within a layer with a finite thickness while in the second case, a vortex sheet is generated. Vortex sheet instability is stronger than that of a vorticity layer. This is similar to the Kelvin–Helmholtz waves growing on a vorticity layer except that for the latter, there is a cutoff wavenumber, above which the waves do not grow. The absence of a cutoff wavenumber in the Rayleigh–Taylor instability is due to the absence of a restoring mechanism for short waves.

IV.4. *Results of the Numerical Simulations*

The simulation of Rayleigh–Taylor instability is performed using the transport-element method for $r_\rho = 2$, 3, The initial perturbation is imposed by displacing the elements in the y-direction in the forms of a cosine wave with a 90° phase angle. The wavelength of the perturbation is $\lambda = 13.2L_0$, where $L_0 = \sqrt{2}\,S$ and S is the standard deviation of the Gaussian curve used to describe the initial density-gradient profile. The amplitude of the perturbation is $\varepsilon = 0.1\lambda$. Calculations were also done for a very small amplitude, $\varepsilon = 0.0005\lambda$, in order to compare the results with the linear theory. The growth rates computed from the numerical simulations in the linear range are shown by the symbols in Fig. 3.

IV.4.1. *Atwood number* = 0.33. The location and velocity of the transport elements are shown in Fig. 4 for $r_\rho = 2$, $A = 0.33$, at $t = 5.0$, 8.0, 10.0, and 11.5. Since the elements are placed on isoscalar material lines, these plots

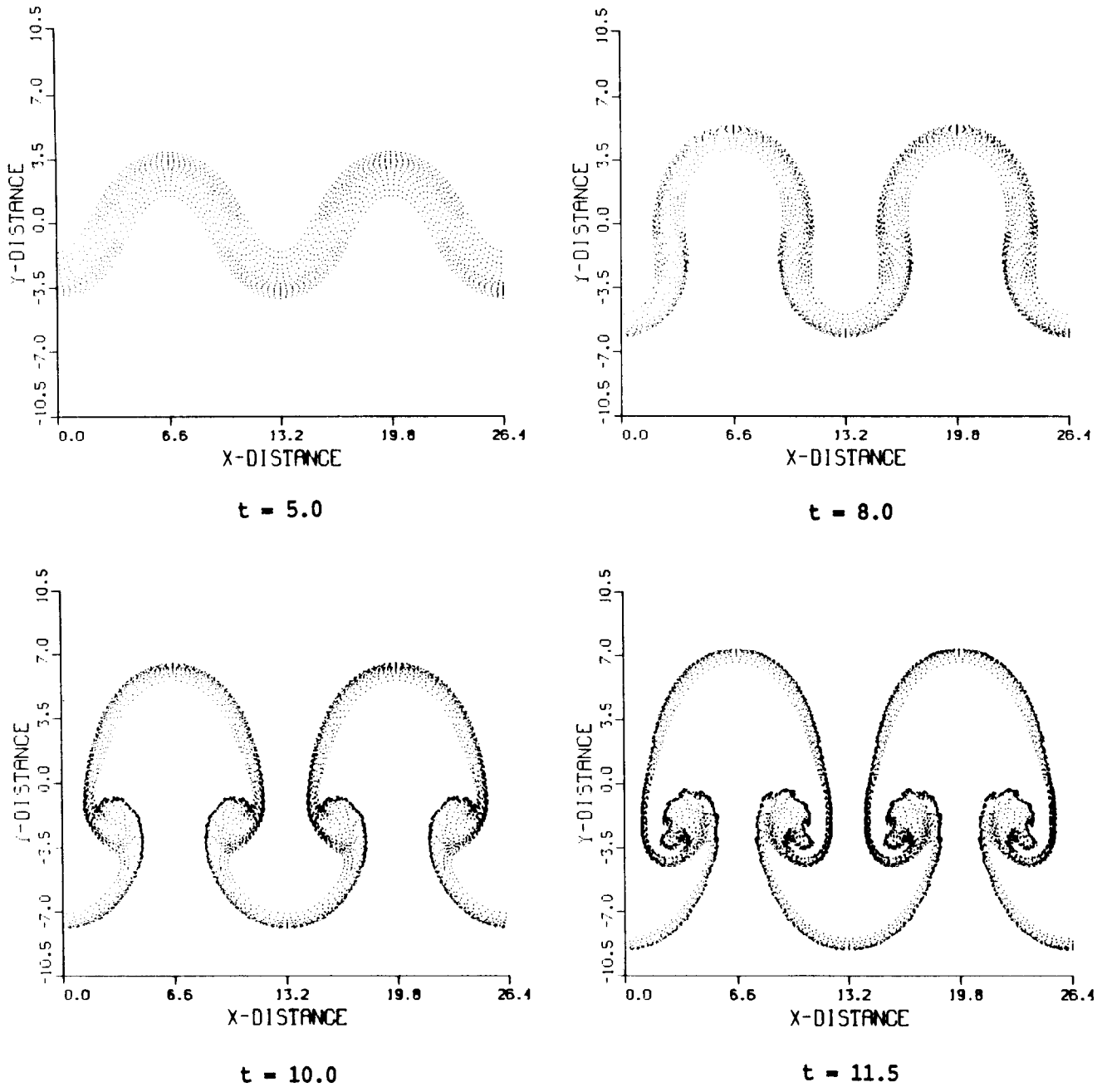

FIG. 4. The locations and velocities of the transport elements at $t = 5.0$, 8.0, 10.0, and 11.5, for $A = 0.33$ ($r_\rho = 2$).

also depict the deformation of the material lines within the layer. Isoscalar lines are obtained by computing the values of the scalar on a square mesh using Eq. (29) and then feeding the data into a standard contour plotting program, as shown in Fig. 5. This process generates contours which do not represent any changes smaller than the grid size used in the plotting. Since the flow is inviscid, the scalar contours could also be obtained by drawing lines connecting transport elements which have the same value of the scalar. The indirect method was used as a check on the accuracy of the scheme. The difference between the value of the scalar computed using the indirect method and its exact value did not exceed 0.1% at the late stages.

The temporal development of the flow can be divided into four stages: (1) the initial perturbation is amplified due to the rise/fall of the light/heavy fluid without appreciable deformation within the layer; (2) the perturbation continues to grow maintaining antisymmetry between the light and heavy fluid but the thickness of the temperature gradient zone starts to change indicating the onset of currents within

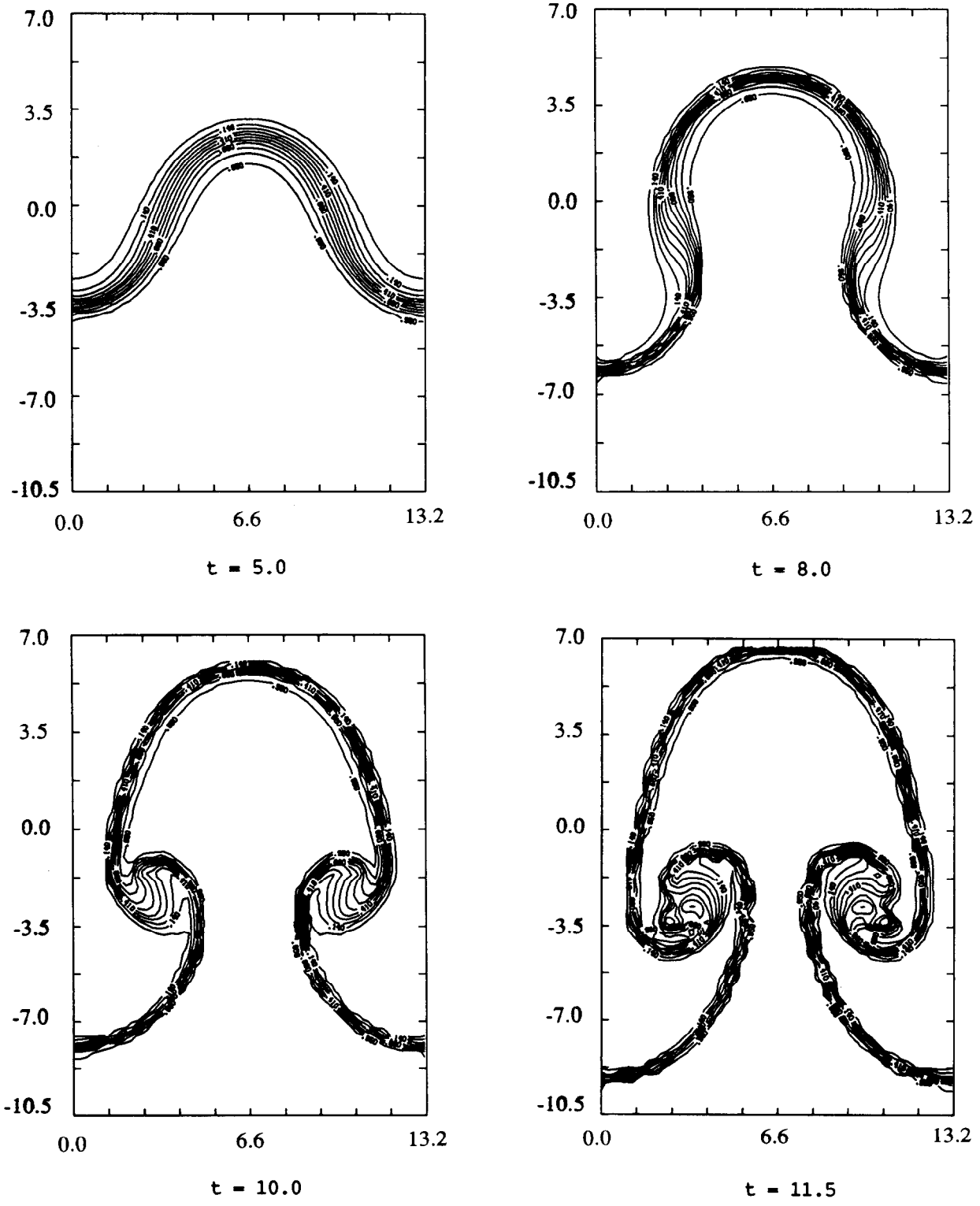

FIG. 5. The normalized temperature contours ($T = 1/\rho$) at $t = 5.0$, 8.0, 10.0, and 11.5, for $A = 0.33$ ($r_\rho = 2$).

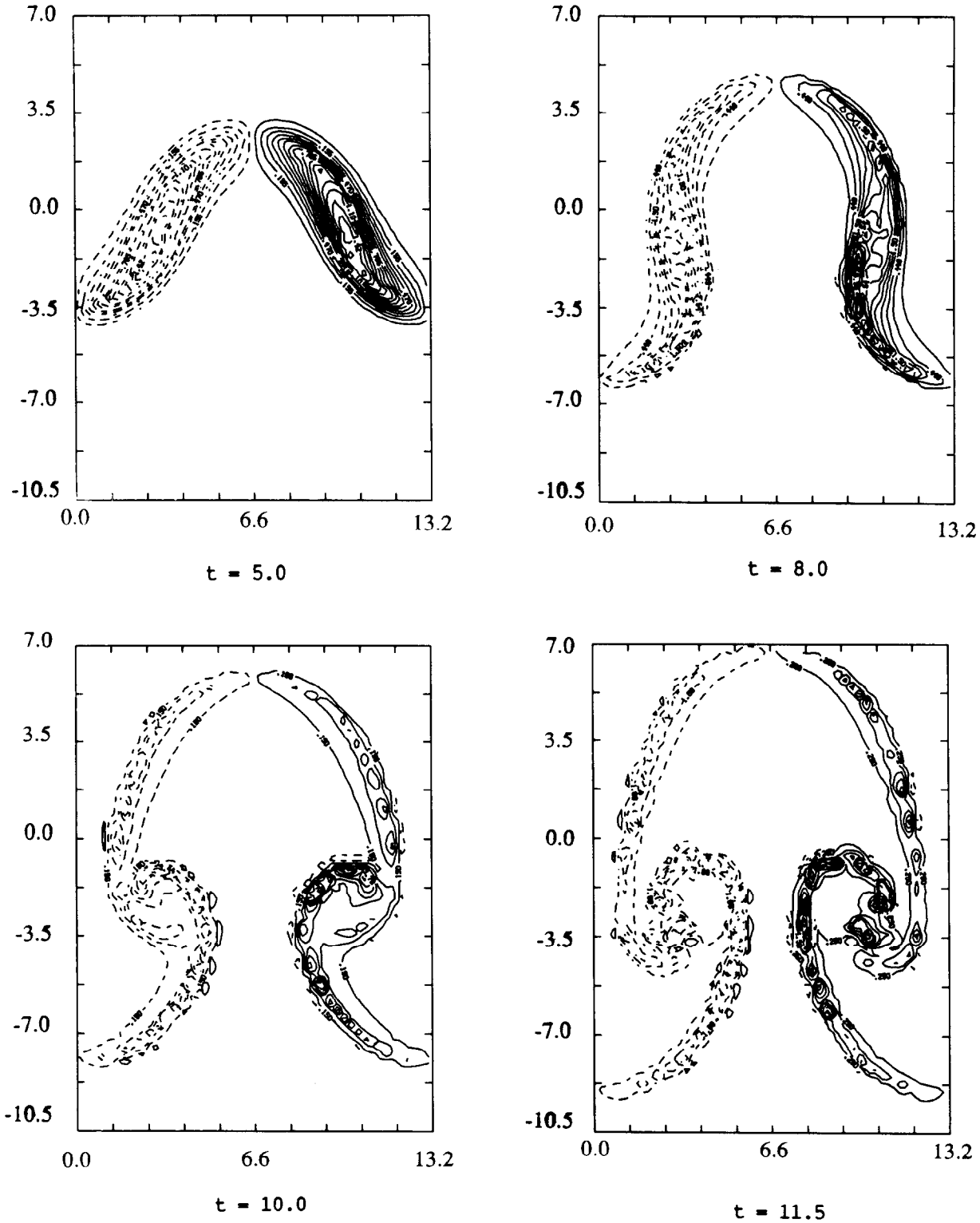

FIG. 6. The streamline contours at $t = 5.0$, 8.0, 10.0, and 11.5, for $A = 0.33$ ($r_\rho = 2$).

the layer; (3) the layer rolls up at the midpoints between the highest and lowest peaks and the fluid originally within the layer migrates towards these points; and (4) the layer continues to roll up forming large eddies which move vertically downwards. At the late stages, the boundaries of the large eddies develop smaller eddies.

The development of the familiar mushroom-shaped instability is observed during the second and third stages, with the layer forming two symmetric structures on both sides of the mushroom. The two eddies develop as a result of an instability which resembles the Kelvin–Helmholtz instability. The symmetry across the vertical line, which was not enforced in the calculations, ensures that the total vorticity in the domain is always zero. The part of the layer that moves into the dense fluid is referred to as the "bubble" and the one that moves into the light fluid is referred to as the "spike." For all values of r_ρ, the simulations were performed until the spike of the high density fluid reached a depth of approximately -10.0 in nondimensional units. Simulations beyond this point required a very large number of elements and a very small time step due to the large strain rate and material acceleration.

The eddies that develop on both sides of the mushroom entrain more of the low-density fluid by volume, as was observed in the case of a variable density shear layer. This is evident from the fact that material layers on the light fluid side undergo more distortion than those on the heavy fluid side (Figs. 4 and 5, $t = 11.5$). The tongue of light fluid

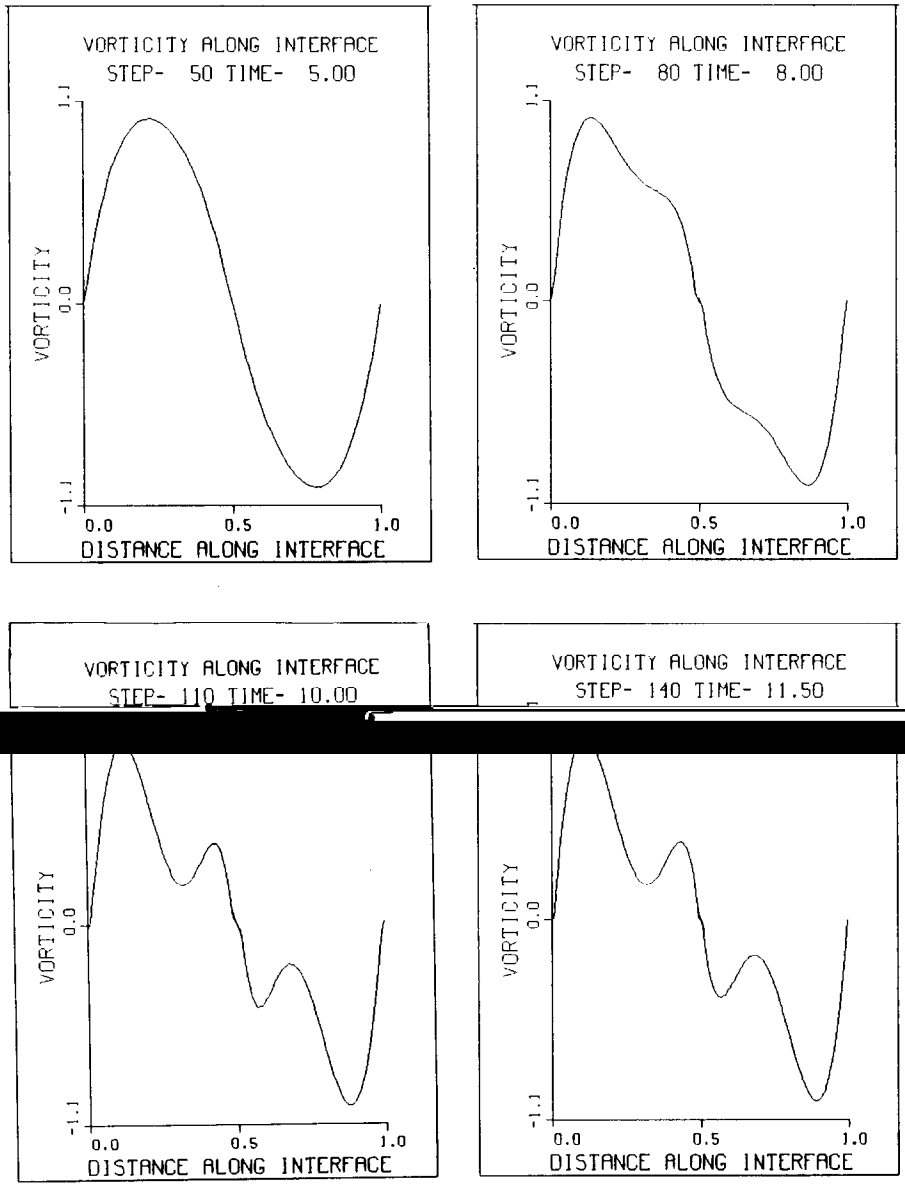

FIG. 7. The least squares fit of the vorticity distribution along the central layer at $t = 5.0$, 8.0, 10.0, and 11.5, for $A = 0.33$ ($r_\rho = 2$).

penetrates further into the large structure than that of heavy fluid. The structures form initially very close to $y=0$. As they grow, the eddies move downwards. The asymmetry of these eddies is connected with the unequal penetration of the bubble and spike into the cold and hot fluids, respectively. The origin of this asymmetry can be best revealed by inspecting the vorticity distribution.

tion takes place according to Eq. (5). At the early stages, the interaction between the gravitational acceleration and the density gradient leads to the generation of positive vorticity on the left side of the domain and negative vorticity on the right side. However, at later times, negative/positive vorticity is generated on the left/right part of the domain, respectively, due to the interaction between the inertial acceleration and the density gradient. Vorticity generated in the braids between the eddies is entrained into their cores during rollup. The maximum values of vorticity occur at the centers of the structures.

At the late stages, the vorticity distribution within each eddy is nonsymmetric around its center. As an example, we take the structure on the right-hand side. Within this structure, gravity-generated vorticity at the initial stages is negative. At later times, the vorticity is higher on the left side than on the right side of the eddy. This is due to the generation of vorticity by the baroclinic term, $\mathbf{a}\times\nabla\rho/\rho$, where $\mathbf{a}$ is the material acceleration. It is easy to demonstrate why this term should be positive on the right upper side of the eddy, thus reducing vorticity due to gravity, $\mathbf{j}\times\nabla\rho/\rho$, while it is negative on the left lower side, thus enhancing the gravity-generated vorticity. This asymmetric distribution of vorticity within the eddy leads to the asymmetric entrainment and the downward motion of the center of the eddy. This kinematical argument will be supported by a dynamical argument in the next few paragraphs.

Figure 7 shows the vorticity distribution along the central layer for $t=5.0$, 8.0, 10.0, and 11.5, respectively. The vorticity and the distance along the layer are normalized by their corresponding maximum values at each time step. The vorticity distribution develops smoothly at the initial stages with peak values occurring at the centers of the rolling structures. At later stages, due to inertial acceleration, the

there are two maxima on both sides of the mushroom. Moreover, vorticity has a higher peak along the inner fold of the mushroom, or the spike, than along the outer edges of the mushroom head, or the bubble. This is because vorticity generation by inertial acceleration is uneven.

As a measure of the growth of the instability, we plot the cumulative circulation in the field in Fig. 8. The positive and negative components of the circulation are summed separately. The circulation increases from its initial value of zero, and equal amounts of positive and negative circulation are generated. The rate of increase of circulation rises after rollup. Another measure of the growth of the instability is the total entrainment into the large structures. This can be determined from the value of the streamfunction of the outermost closed contour, or from the total length of the material layer. Figure 9 shows the streamlines over a single wavelength of the perturbation. The volumetric entrainment into the large structures is indicated by the increase in the number of closed streamlines around the center of the structure. The central vertical streamline is assigned a value of zero so that the streamfunction at the center of the structure can be used as a measure of volumetric entrainment. The nondimensional streamfunction at the core of the eddy at $t=11.5$ is $\psi_0=7.85$.

The straining of the material lines with the growth of the instability is shown in Fig. 10. The mean length of the "interface," defined as the total length of all the material layers

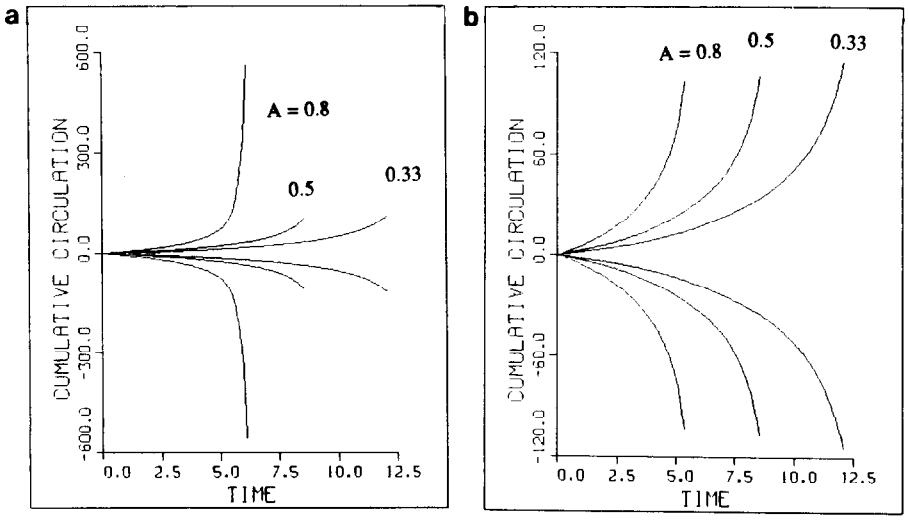

FIG. 8. (a) The cumulative circulation in the flow field. The positive and the negative components are summed separately; (b) same as in (a) but on different scales.

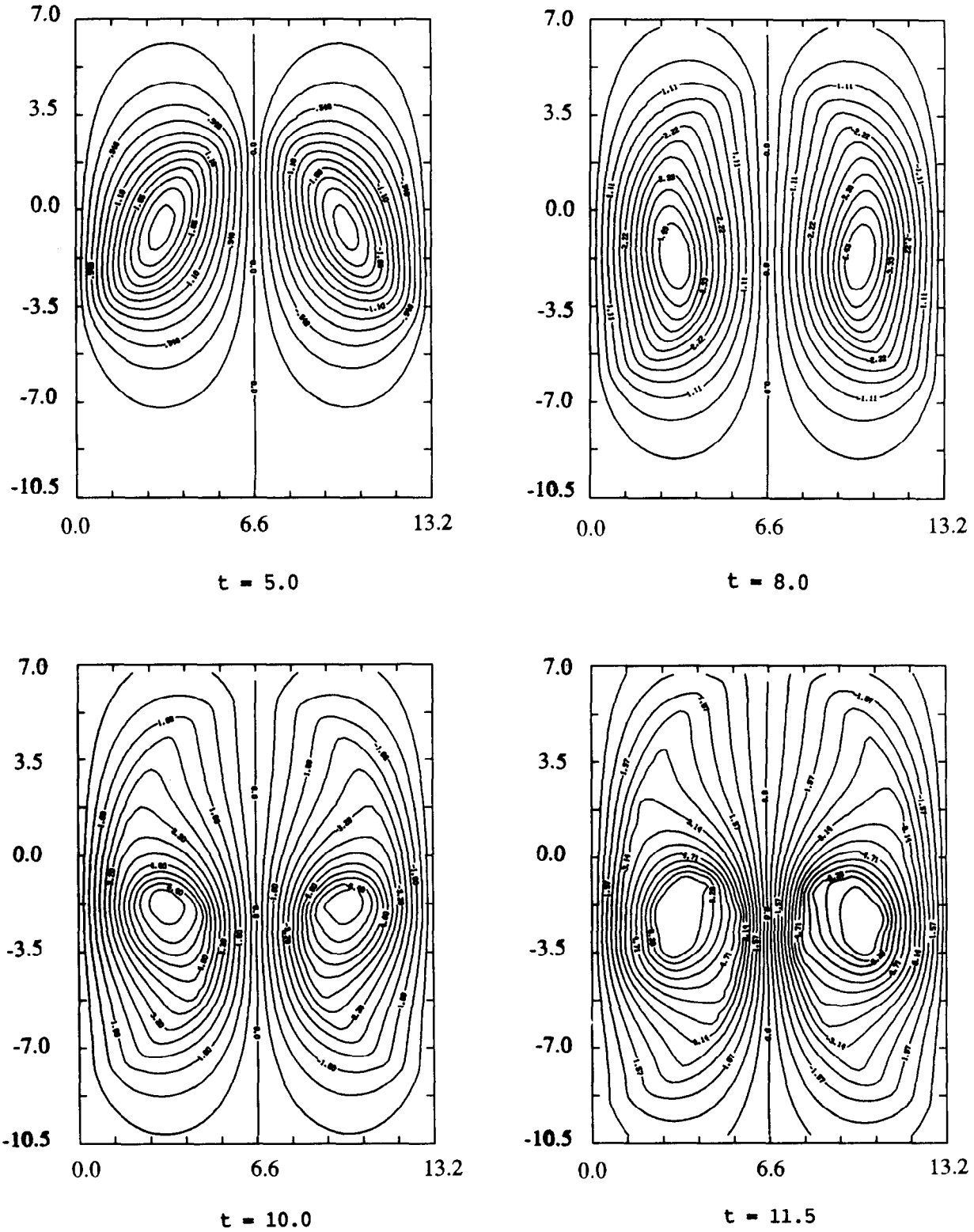

FIG. 9. The vorticity contours at $t = 5.0$, 8.0, 10.0, and 11.5, for $A = 0.33$ ($r_\rho = 2$). Broken lines represent positive vorticity and solid lines represent negative vorticity.

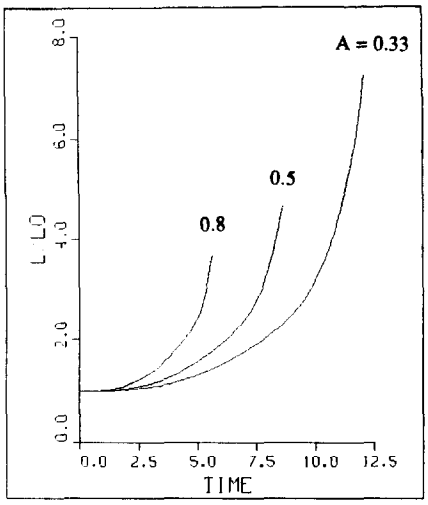

FIG. 10. The normalized mean length of the material layers.

used in the calculations normalized by their length at $t = 0$, is shown as a function of time. The length of the interface at $t = 11.5$ is about seven times the initial length (15λ). The slope of the curve grows with time, indicating that the rate of elongation, or average strain, increases.

The evolution of the flow is shown by positions of the highest and lowest points at both the highest section of the bubble and the lowest section of the spike, in Fig. 11a. To compare the results of the finite-thickness layer with those of the infinitely thin interface, we show the mean average of the extreme positions of all the computational layers at the top of bubble and the bottom of the spike in Fig. 11b (since 15 layers are used, each point represent an average over 15 y-locations). The motion of both sections of the waves, the spike and the bubble, grows unequally beyond the linear range. The strain associated with the rollup of the large eddies reduces the thickness of the layer at these extreme positions. The thinning of the layer is associated with the generation of internal currents, or the entrainment of the fluid into the large eddies.

Figure 12 shows the highest absolute values of (a) the bubble and (b) spike velocities, obtained by calculating the vertical velocity at the tips of the two structures (representing the derivatives of the continuous lines in Fig. 11a). In Fig. 13, velocities at (a) the top of the bubble and (b) the bottom of the spike, obtained as an average over the velocities of all the layers within the extremes of the bubble and the spike, are shown. The mean bubble velocity reaches an asymptotic value around $t \sim 7$, while the mean spike velocity reaches its asymptotic value around $t \sim 7.5$. Moreover, the mean spike velocity is higher than that of the bubble. The reason for this is described next.

We have presented a kinematical argument to explain the asymmetry between the bubble and the spike on the basis of the vorticity generation mechanism. This argument is now extended to explain the difference between the bubble and the spike velocities. As indicated in Fig. 4, the eddies are pushed downward towards the spikes. Thus the velocity induced on the latter is smaller than that induced on the former. While we prefer this argument, the following dynamical argument, which is based on the similarity between the flow around the bubble and the spike and that of a separated flow around a bluff body, was offered in the literature [18]. The pressure drag on these virtual bodies is proportional to the size of the body, defined approximately by the radius of curvature, the density of the medium it is moving into, and the velocity of the body. Results show that the size of the bubble is slightly larger than that of the spike and it is moving into a denser fluid. Thus, the pressure drag

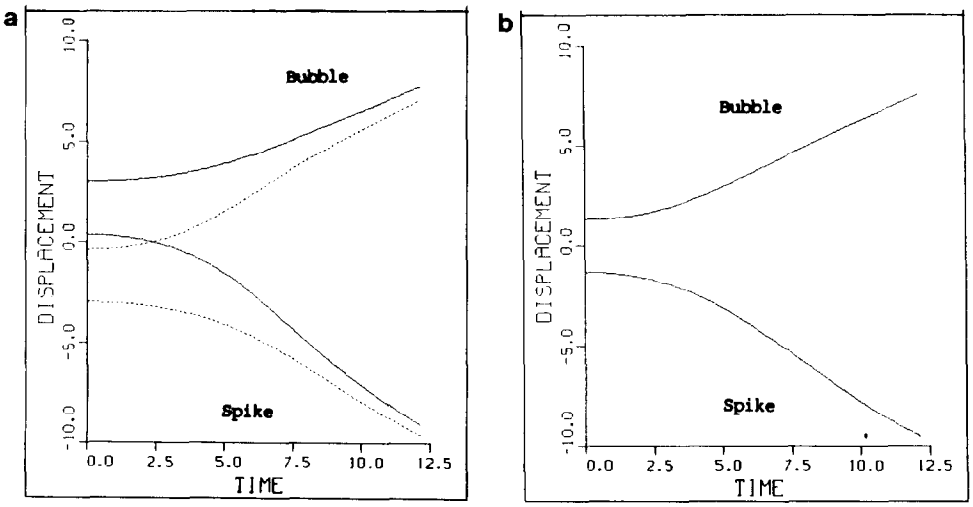

FIG. 11. (a) The highest and lowest positions of the bubble and the spike as a function of time for $A = 0.33$ ($r_\rho = 2$). The highest position is shown by the continuous curve and the lowest position by the broken curve. (b) The mean positions of the bubble and the spike for $A = 0.33$ ($r_\rho = 2$).

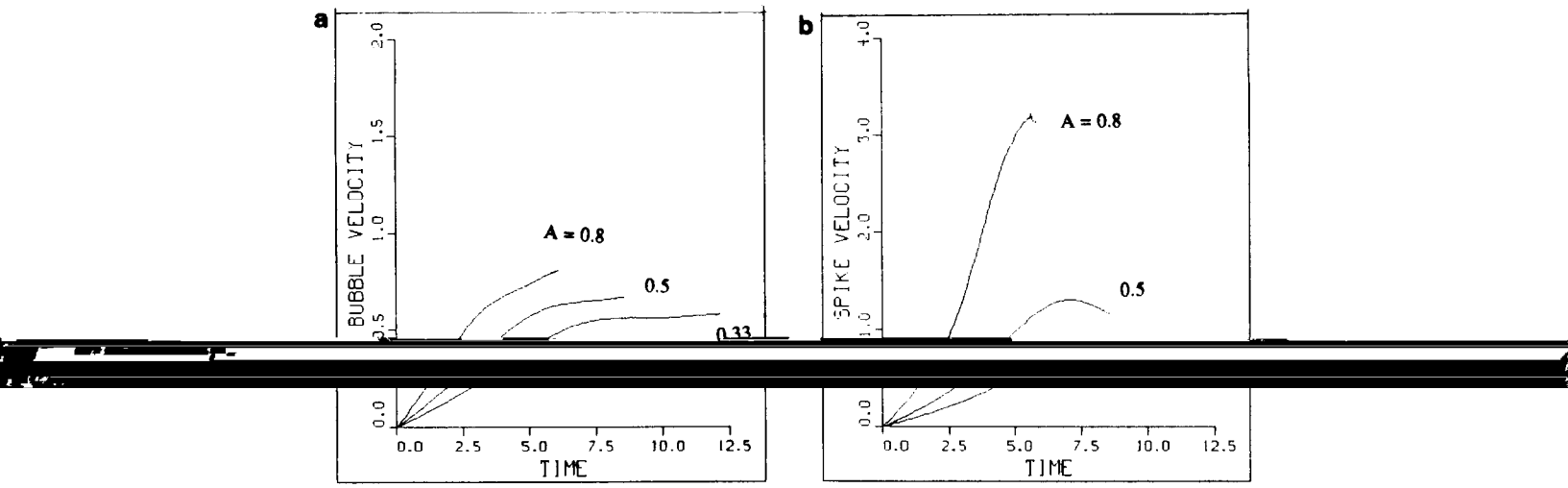

FIG. 12. (a) The velocity at the highest point of the bubble; and (b) the velocity at the lower point of the spike.

on the bubble is larger than the drag on the spike, its velocity is smaller, and it reaches its asymptotic value faster than the spike.

The normalized asymptotic mean value for the bubble velocity $U_{bn} = U/(\sqrt{\lambda}) = 0.29$. Kerr [10] obtained $U_{bn} = 0.27$ for a density interface using a vortex sheet method. The discrepancy between the tip and the mean value of the bubble velocity can be attributed to the relative motion of the material layers during the growth of the instability. Experimentally, the asymptotic bubble velocity is found to be between 0.2 and 0.3 [8]. The peak value of the normalized mean spike velocity is $U_{sn} = 0.45$, occurring at $t = 7.5$ (Fig. 12b). The value obtained in Ref. [10] is $U_{sn} = 0.44$, occurring at $t = 8.5$. The latter is close to our computed value, 0.435, for the spike tip, shown in Fig. 12b. It is interesting to note that these values are independent of the perturbation wavelength.

IV.4.2. *Atwood number* = 0.5. The location and velocity of the transport elements for $r_\rho = 3$, $A = 0.5$, is shown in Fig. 14 at $t = 5.0$, 7.0, 7.85, and 8.6. Compared to the case $A = 0.33$, we observe the following: (1) The instability develops faster; the tip of the spike reaches $y = -10.0$ at $t = 8.6$, as predicted by the linear theory. (2) The extent of the rollup is decreased. (3) The size of the bubble is much larger than that of the spike, i.e., the symmetry of the flow is enhanced at higher density ratios. (4) The structures are formed at a lower elevation. (5) More of the light fluid is entrained into the eddies than of the heavy fluid. These changes can be explained by analyzing the vorticity distribution (not shown) and are connected with the baroclinic vorticity generated in the nonlinear stages of the instability.

Similar to the previous case, vorticity of the opposite sign to the gravity-generated vorticity is created by the

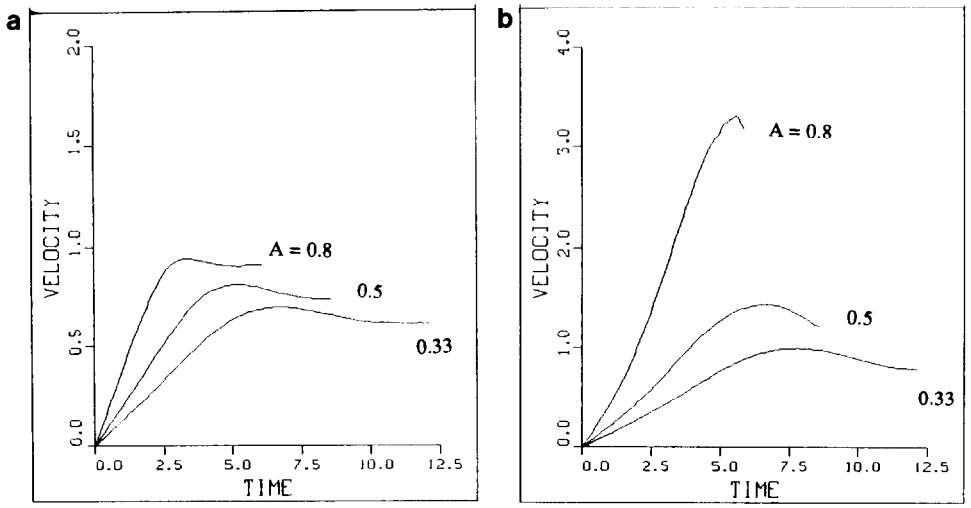

FIG. 13. (a) The mean velocity at the top of the bubble; (b) the mean velocity at the bottom of the spike.

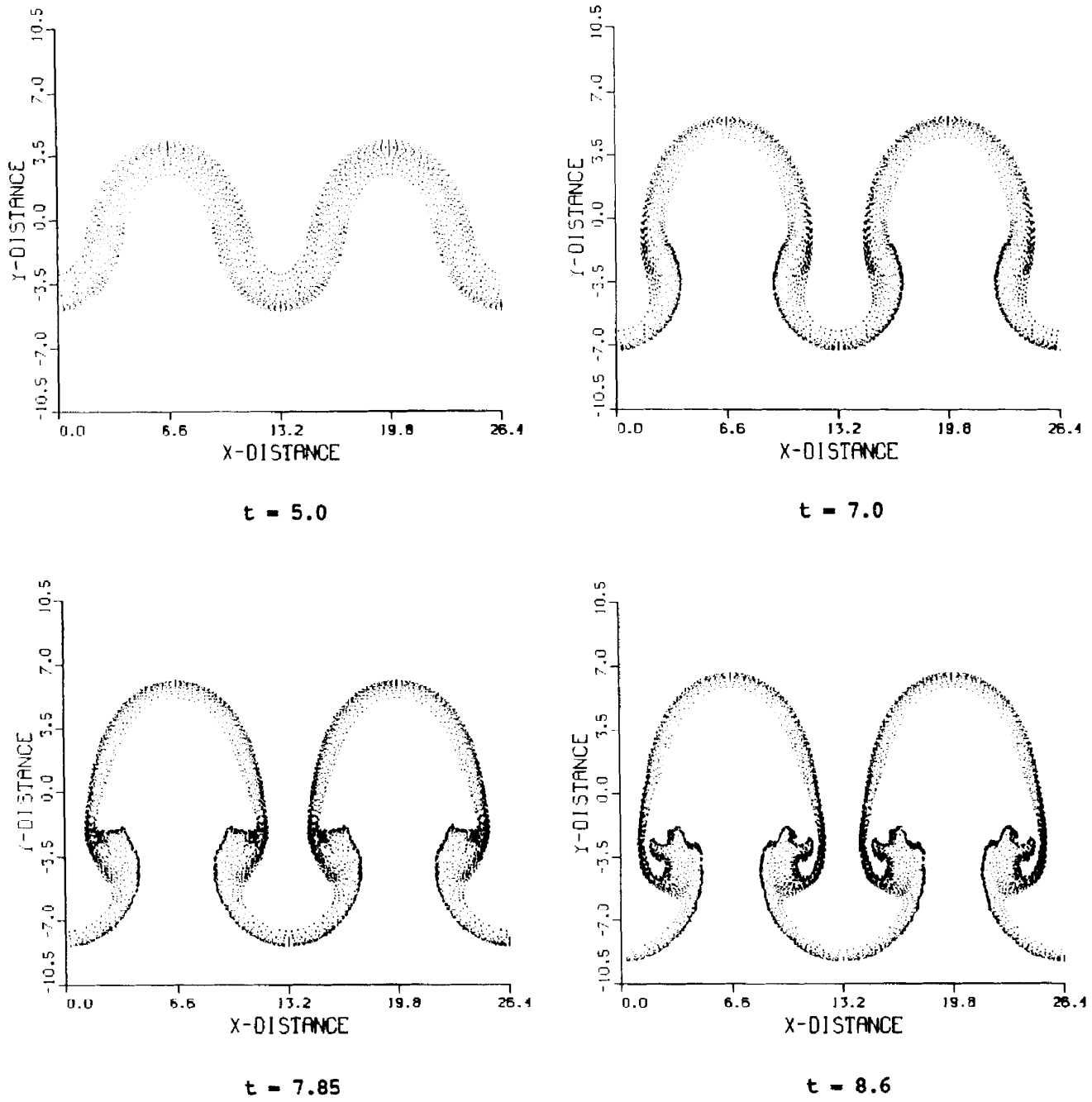

FIG. 14. The locations and velocities of the transport elements at $t = 5.0$, 7.0, 7.85, and 8.6, for $A = 0.5$ ($r_\rho = 3$).

baroclinic torque on the bubble side of the mushroom and with the same sign of the gravity-generated vorticity on the spike side. Thus, higher vorticity is established in the inner side of the eddies than in the outer side. The asymmetric vorticity distribution generates a finite convective velocity that forces these eddies downwards towards the light fluid. This, as will be shown later, is a non-Boussinesq effect. Results of this case will be discussed further in Section IV.4.4, in connection of results of the Boussinesq approximation.

Volumetric entrainment, as obtained from the value of the streamfunction at the center of the eddy, is higher than in the first case, $\psi_0 = 9.3$ at $t = 8.6$. Entrainment is larger despite the fact that the rollup has been reduced. The temperature contours confirm that more light fluid is ingested into the cores than heavy fluid and that the entrainment ratio increases for larger values of A. The distance between the same scalar contours within the region of the spike is smaller than within the region of the bubble. This, as shown in the previous section, is due to the accumulation of

vorticity in the lower part of the mushroom leading to higher strains within the spike.

The asymptotic mean bubble velocity, shown in Fig. 13a, is $U_{bn} = 0.255$ which compares well with the value of 0.26 obtained in Ref. [9] in the simulation of an RT instability of a density interface using the vortex-in-cell method. A possible reason for this agreement is that vortex-in-cell computation introduces a numerical finite thickness in the simulations of a infinite interface. Although the calculations had to be stopped before the spike could attain its asymptotic velocity, the peak spike velocity is $U_s = 1.3$ which corresponds to $U_{sn} = 0.5$. The peak spike velocity obtained in Ref. [9] is $U_{sn} = 0.48$.

IV.4.3. *Atwood number* = 0.8. The location and velocity of the transport elements are shown in Fig. 15 at $t = 3.0$, 4.25, 4.75, and 5.25. The spike reaches $y = -10.0$ at $t = 5.25$. The fast penetration of the spike into the light fluid allows little time for the rollup of the structures due to the KH instability (as the density ratio approaches infinity, i.e.,

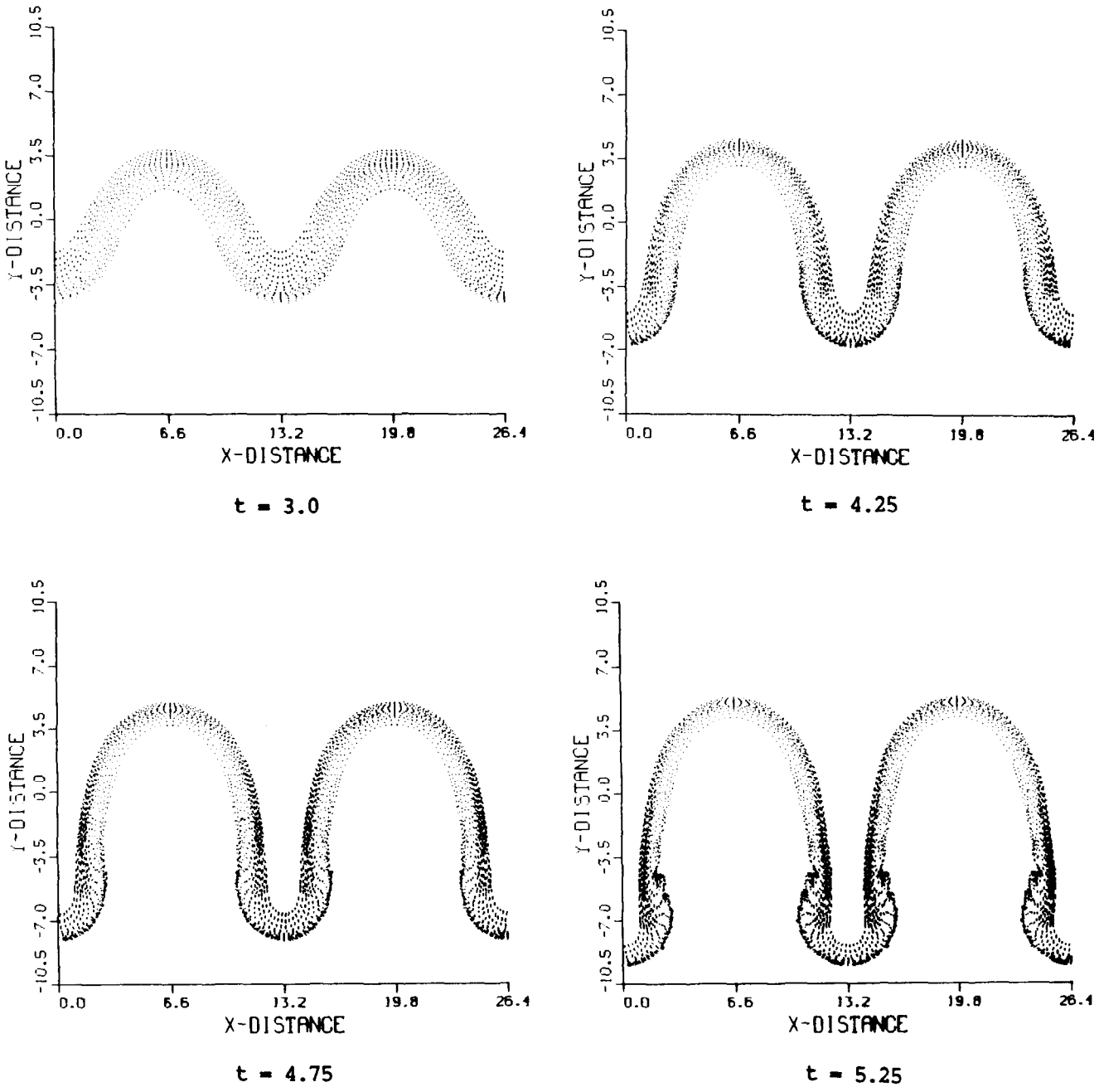

FIG. 15. The locations and velocities of the transport elements at $t = 3.0$, 4.25, 4.75, and 5.25, for $A = 0.8$ ($r_\rho = 9$).

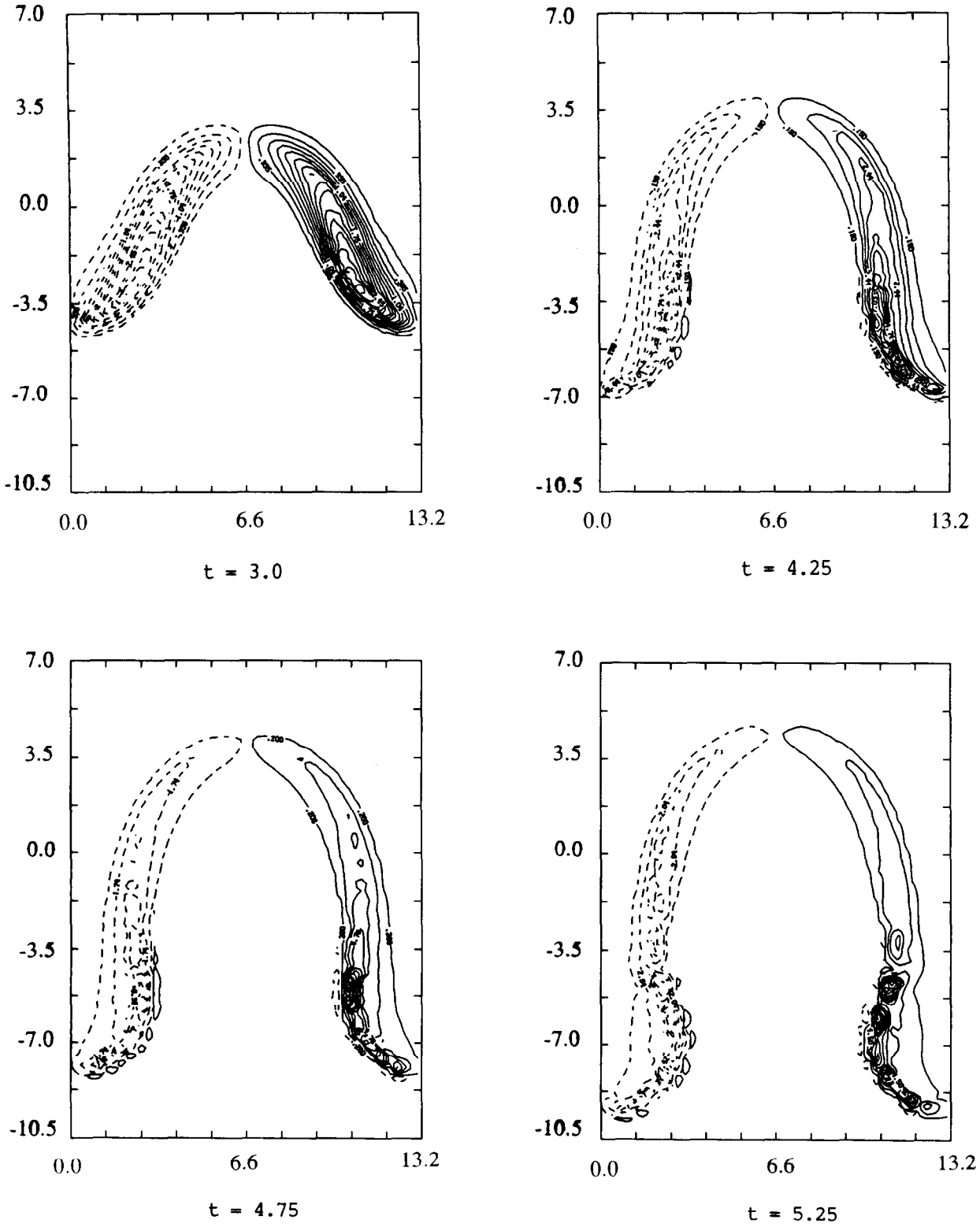

FIG. 16. The vorticity contours at $t = 3.0, 4.25, 4.75$, and 5.25, for $A = 0.8$ ($r_\rho = 9$). Broken lines represent positive vorticity and solid lines represent negative vorticity.

the case of a free fall of a fluid into vacuum, the net pressure everywhere in the field thus preventing rollup). It appears that gravity, in a strongly accelerating flow at high density ratios, acts to stabilize the KH instability. The bubble is larger than the spike and the rollup instability forms at a lower elevation as compared to previous cases. Furthermore, higher gradients are formed within the spikes. The intensification of scalar gradients within the spike leads to numerical complications, and higher temporal and spatial resolutions must be provided.

Figure 16 shows the vorticity contours. As in previous stronger along the sides of the spike. A steep gradient of vorticity forms as vorticity generation within the spike intensifies. This is shown by the vorticity distribution along the central layer depicted in Fig. 17. This situation, which resembles a shockwave in gas dynamics, makes it very expensive to continue the calculations beyond $t = 5.25$. The number of transport elements added along individual layers to capture the strain field exceeds that used in the previous cases. The vorticity in regions other than that of the spike is

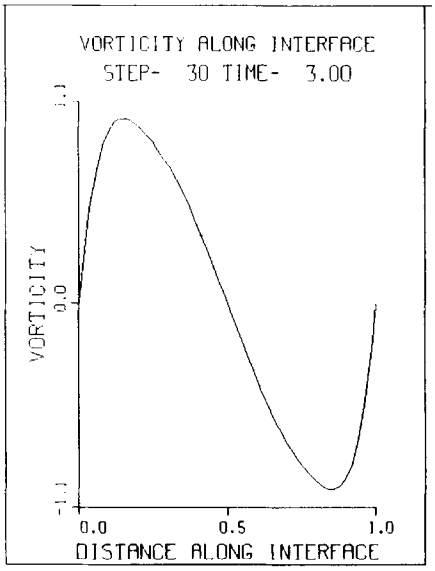

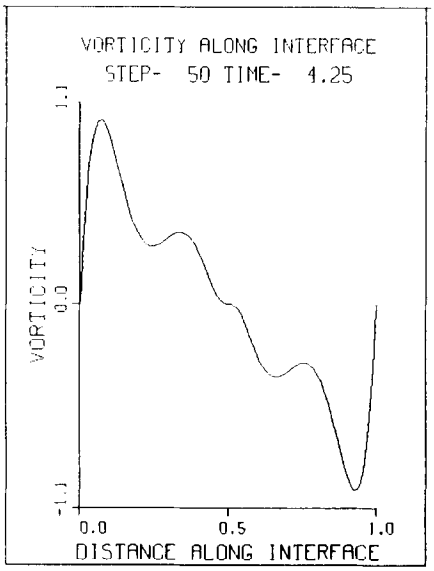

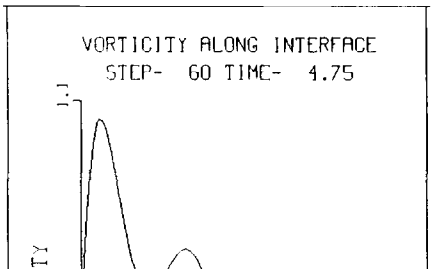

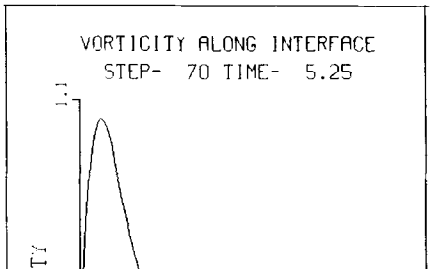

nearly zero. This asymmetry is due to the effect of the baroclinic torque that alternately opposes and enhances the existing vorticity in the bubble and the spike, respectively.

Figure 18 shows the streamline plots. Although there is little rollup, the entrainment, as indicated by the amount of fluid circulating around the eddy center increases. The streamfunction at the center of the structure at $t = 5.25$ is $\psi_0 = 9.75$. The migration of the structure to lower elevations is clearly observed from the streamline contours.

The mean velocity of the bubble at the final time from Fig. 13a is $U_{bn} = 0.27$. The value obtained by Kerr [9] for $r_\rho = 9$ is 0.23. This is close to our value for the tip velocity, shown in Fig. 12a, $U_{bn} = 0.235$. The computation of the RT instability of a thin interface evidently produces results

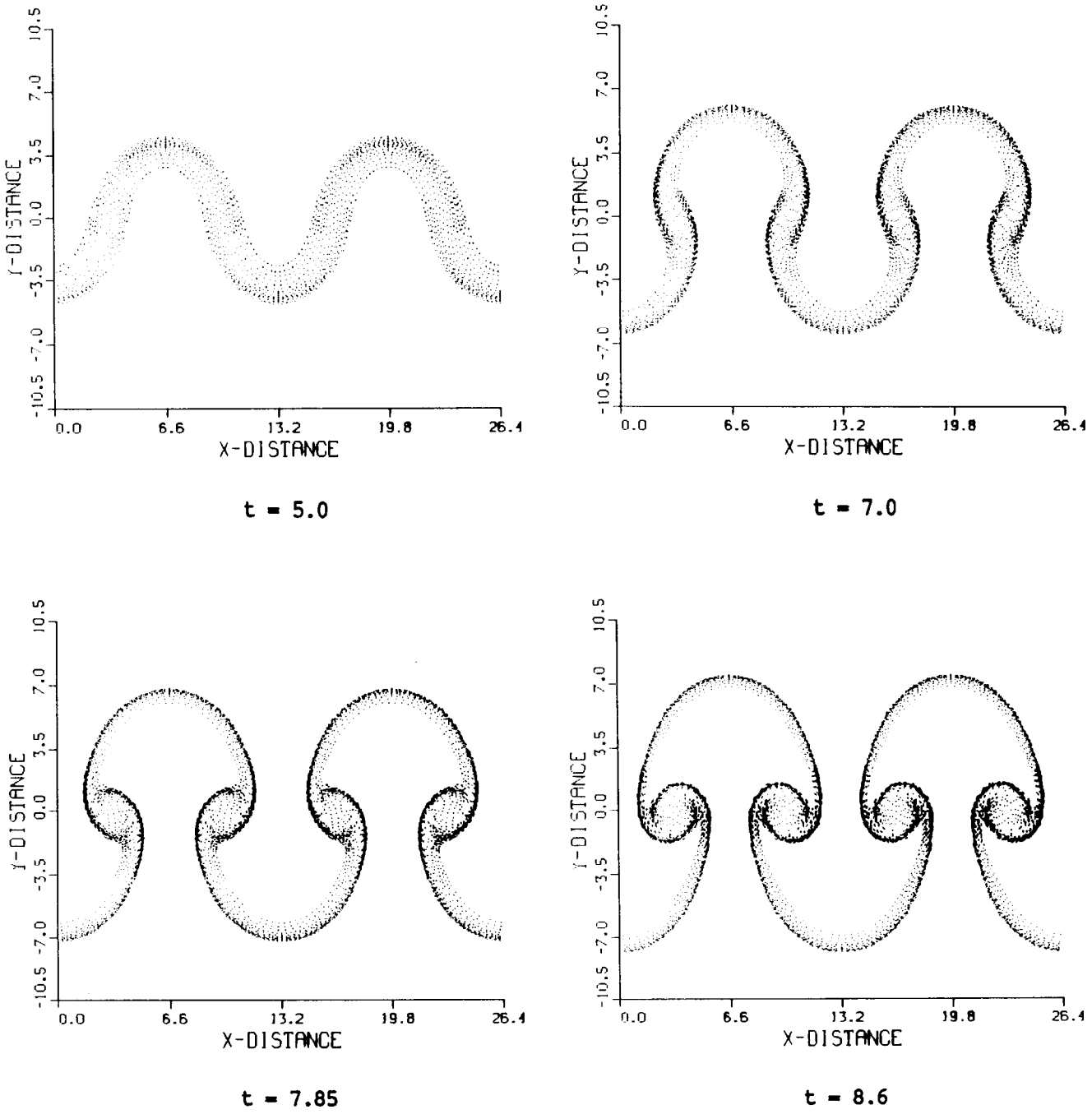

FIG. 19. The locations and velocities of the transport elements at $t = 5.0$, 7.0, 7.85, and 8.6, for $A = 0.5$ ($r_\rho = 3$) using the Boussinesq approximation.

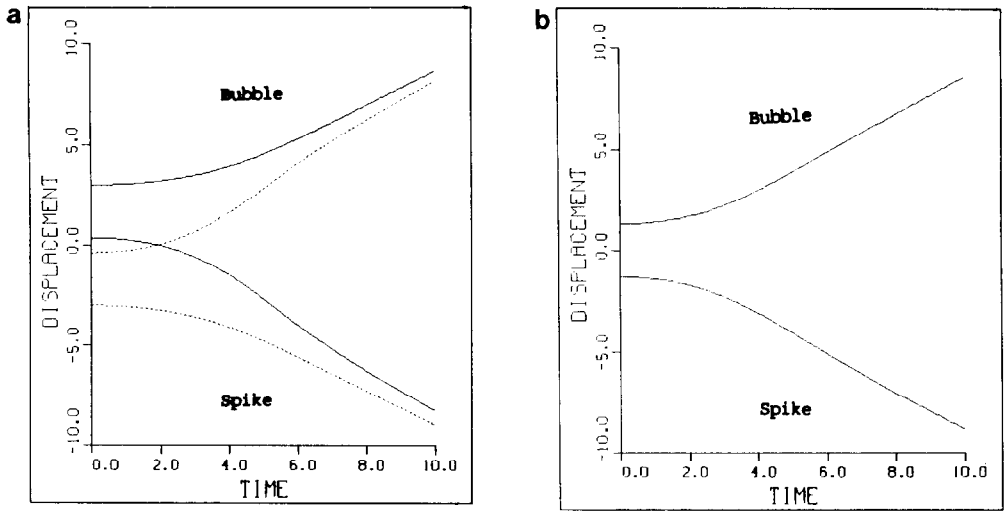

FIG. 20. (a) The positions of the highest (solid lines) and the lowest points (broken lines) on the bubble and spike; and (b) the mean positions of the bubble and spike for $A = 0.5$ ($r_\rho = 3$).

which match the results of our computations of the extreme points of the layer. In the limit, as r_ρ approaches infinity, the spike would have a constant acceleration equal to that of gravity, i.e., the slope of the curve would be unity. For $r_\rho = 9$, the slope of the curve from Fig. 13b is 0.94.

IV.4.4. *Atwood number = 0.5 with Boussinesq approximation.* This approximation is implemented by neglecting the effect of inertial acceleration, $d\mathbf{u}/dt$, with respect to the gravitational acceleration. The simulations are performed for $r_\rho = 3$, $A = 0.5$. The locations and velocities of the vortex elements are shown in Fig. 19 at the same times as in Fig. 14. Neglecting the inertial terms leads to a symmetric growth of the structures which remain centered at $y = 0$. Concomitantly, equal volumes of the heavy and the light fluids are entrained into the eddies, and the spike and bubble penetrate equally into the heavy and light fluids, respectively.

The symmetry of the motion of the bubble and the spike is shown further by Fig. 20, where the vertical displacement of the two bounding layers of the variable density fluid on both the bubble and the spike sides are shown. Shown also is the average location of all the computational elements at the top of the bubble and the bottom of the spike. Both plots confirm the symmetry between the two sections of the wave in the absence of baroclinic vorticity generation, contrary to what is revealed in Fig. 11, namely that in the non-Boussinesq approximation, the two sections of the wave grow asymmetrically beyond the linear range (it should be mentioned here that in the non-Boussinesq approximation, while the trend is the same, the asymmetry between the bubble and the spike is exaggerated as the density ratio between the two streams increases).

A very small asymmetry between the motion of the two sections, not detectable in Fig. 20, is indicated by Fig. 21, where the mean velocities of the bubble and the spike are shown. The small difference between the motion of the bubble and the spike can be attributed to the difference between the density of the layers in the two sections (note that in our calculations, the vorticity generation term in this case is $(-\nabla\rho \times j/\rho)$, not $(-\nabla\rho \times j/\rho_m)$ as in the conventional Boussinesq approximation, which leads to some difference between the rate of vorticity generation in the bubble and the spike).

As indicated before, a kinematical argument based on vorticity generation and distribution can be used to explain

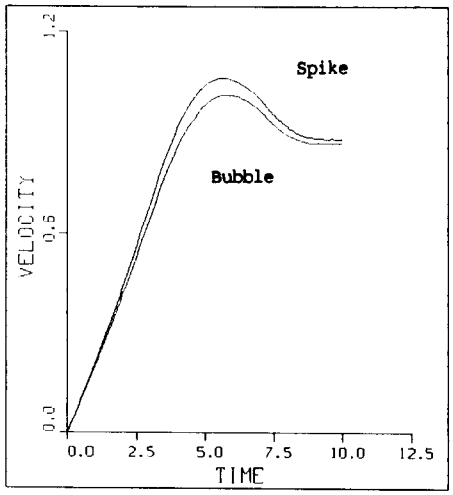

FIG. 21. The mean bubble and spike velocity as a function of time for $A = 0.5$ ($r_\rho = 3$), using the Boussinesq approximation.

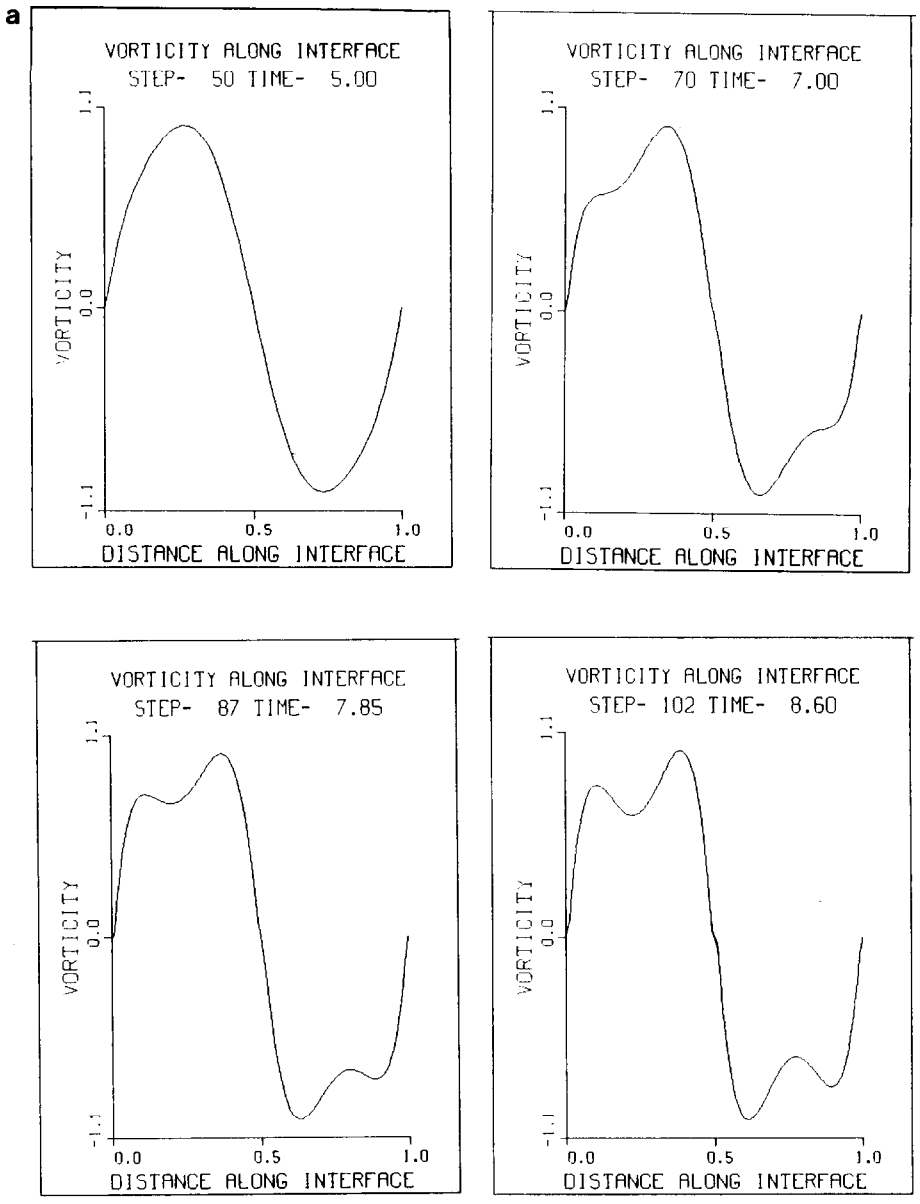

FIG. 22. The least squares fit of the vorticity distribution along the central layer at $t = 5.0, 7.0, 7.85$, and 8.6 for $A = 0.5$ ($r_\rho = 3$): (a) using Boussinesq approximation; (b) without using Boussinesq approximation.

these observations. Vorticity distribution along the central layer in the Boussinesq and non-Boussinesq approximation, and b, respectively. In the former, the maximum absolute values of the vorticity on the spike and the bubble are almost equal. The small difference between the two peaks is due to the difference in density among the layers. Since baroclinic effects are absent, gravity generated vorticity is not counteracted by the baroclinic vorticity thus leading to a symmetric distribution. This maintains higher vorticity in the bubble than in the spike. On the other hand, because of baroclinic vorticity generation due to inertial acceleration in the non-Boussinesq case, the vorticity is higher within the spike than the bubble, as shown in Fig. 22b.

V. CONCLUSIONS

Simulations of the Rayleigh–Taylor flow generated within a material layer, across which finite temperature gradients exist, are reported. Simulations are performed using the transport-element method; a grid-free Lagrangian field method constructed on the basis of the accurate discretization of flow gradients among finite area elements, and the transport of these elements along particle trajectories.

b

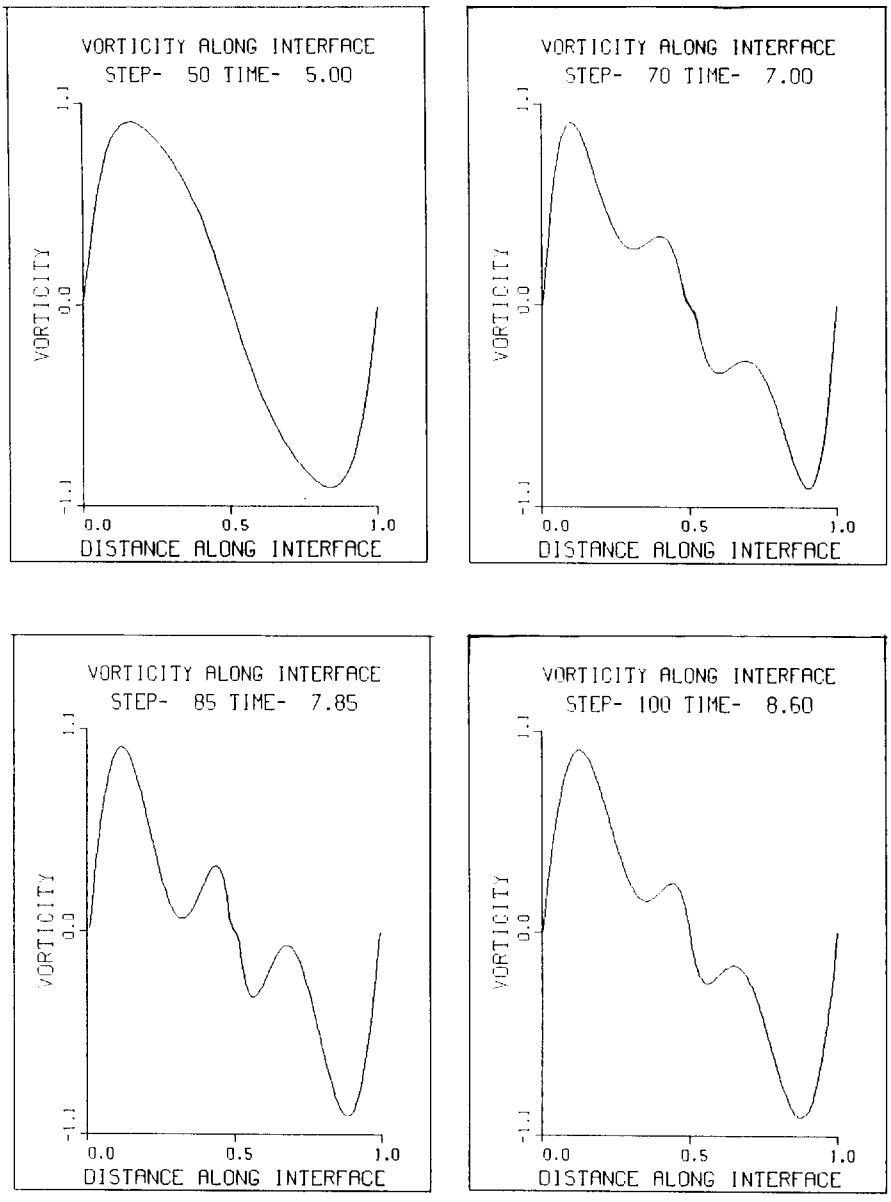

FIGURE 22—*Continued*

The method is adaptive by construction. Gradient transport is made conservative by relating the changes in the local gradients to the distortion of the flow map via kinematical relations. The method captures the generation of small scales and strong scalar gradients by maintaining the distance between neighboring elements in the direction of principle strain below a maximum value and by reducing the core size of the elements to conserve the material area. Inertial acceleration is used to monitor vorticity generation.

Solutions at the early stages of development are validated by comparing the predictions of the initial growth rate of the numerical simulation to the results of the linear stability theory of a finite thickness Rayleigh–Taylor flow. These solutions are also used to show the effect of the layer thickness on its stability properties. Solutions at the late stages are compared with numerical results reported previously for the case of a thin sheet approximation when possible. These solutions are used to show the effect of the baroclinic vorticity generation on the flow.

Within the nonlinear stages, we find that entrainment currents are generated within the material layer between the highest and the lowest temperature contours. The strength of these currents, which lead to the amalgamation of the vorticity generated within the layer into large structures on the two sides of the evolving mushrooms, is proportional to the density ratio. This amalgamation process may or may

not be accompanied with a rollup depending on the density ratio. The asymmetry of the large structures which form on both sides of the mushroom is attributed kinematically to the inertial, or baroclinic, forces. This is the major contribution of non-Boussinesq effects. The entrainment associated with the formation of the structures is the primary mechanism of mixing in Rayleigh–Taylor flow.

APPENDIX: DERIVATION OF EQS. (23) AND (25)

In an inviscid incompressible flow, the motion of a non-diffusive non-reactive scalar s is governed by

$$\frac{ds}{dt}=0. \tag{A1}$$

The conservation equation of the scalar gradient $g=\nabla S$ can be derived by taking the gradient of Eq. (A1), using the vector identity: $\nabla(A\cdot B)=A\cdot\nabla B+B\cdot\nabla A+A\times(\nabla\times B)+B\times(\nabla\times A)$, and noting that $\nabla\times g$ vanishes identically:

$$\frac{dg}{dt}=-g\cdot\nabla u-g\times\omega. \tag{A2}$$

Thus, s remains constant along a particle path while g changes due to stretch and rotation by the local strain field and the vorticity, respectively. Equation (A2) can be directly integrated to yield the new values of the g_i's,

$$\frac{dg_i}{dt}=-g_i\cdot\nabla u_i-g_i\times\omega_i. \tag{A3}$$

In what follows, we construct an alternative scheme for updating g_i's which avoids computing ∇u at the center of the elements and the numerical integration of Eq. (A3).

Let $g=n\,|g|$, where $n=g/|g|$. We have

$$\frac{d(|g|^2)}{dt}=2\,|g|\,\frac{d\,|g|}{dt}=\frac{d(g\cdot g)}{dt}=2g\cdot\frac{dg}{dt},$$

which implies that

$$\frac{d\,|g|}{dt}=n\cdot\frac{dg}{dt}.$$

Expanding dg/dt,

$$\frac{dg}{dt}=\frac{d(n\,|g|)}{dt}=|g|\,\frac{dn}{dt}+\frac{d\,|g|}{dt}\,n \tag{A4}$$

and, using Eq. (A3), Eq. (A4), and noting that $n\cdot(g\times\omega)=0$,

$$\frac{dn}{dt}=-n\cdot\nabla u-n\times\omega+(n\cdot(n\cdot\nabla u))n. \tag{A5}$$

Let l be the unit normal to n. In Eq. (A5), we decompose the vector $n\cdot\nabla u$ into its components along n and l:

$$\frac{dn}{dt}=-(l\cdot(n\cdot\nabla u))\,l-n\times\omega.$$

Next, we decompose ∇u into its symmetric and anti-symmetric parts, $\nabla u=\nabla u^s+\nabla u^a$:

$$\frac{dn}{dt}=-(l\cdot(n\cdot\nabla u_s))l-(l\cdot(n\cdot\nabla u^a))l-n\times\omega.$$

Since $n\cdot\nabla u^a=-n\times\omega/2$ is in the direction of l, then

$$\frac{dn}{dt}=-(l\cdot(n\cdot\nabla u^s))l-\frac{n\times\omega}{2}. \tag{A6}$$

Equation (A6) shows that the change of the unit normal of the scalar gradient can be decomposed into a solid body rotation, expressed locally in terms of the magnitude of the vorticity, and a pure shear, expressed in terms of the symmetric part of the rate of strain tensor. An expression for the variation of the magnitude of the scalar gradient $|g|$ can be derived using the expansion of dg/dt and Eq. (A5),

$$\frac{d\,|g|}{dt}\,n=-|g|\,(n\cdot\nabla u+n\times\omega+\frac{dn}{dt},$$

which yields

$$\frac{d\,|g|}{dt}\,n=-|g|\,(n\cdot(n\cdot\nabla u))n. \tag{A7}$$

Equation (A7) shows that the magnitude of the gradient changes according to the amount of deformation in the direction of the gradient. In what follows, we relate $d(|g|)/dt$ to the straining of a material element initially in the direction normal to g.

The variation of a small material vector $\delta 1$ is governed by the equation

$$\frac{d\delta l}{dt}=\delta l\cdot\nabla u, \tag{A8}$$

and if δl is chosen to lie on a surface of constant s at $t=0$. Equation (A1) implies that δl will always remain on this surface. If l' denotes the unit vector in the direction of δl,

then $n \cdot l' = 0$ at all times, i.e., $l' = l$. If we now decompose δl as $\delta l = |\delta l|\, l$, a similar procedure to that for g yields the expressions

$$\frac{d|\delta l|}{dt} = l \cdot \frac{d\delta l}{dt} \tag{A9}$$

and

$$\frac{dl}{dt} = l \cdot \nabla u - (l \cdot (l \cdot \nabla u))l \tag{A10}$$

which are analogous to Eqs. (A4) and (A5). We solve for $d(|\delta|)/dt$ from Eqs. (A9) and (A10) to obtain

$$\frac{d|\delta 1|}{dt} l = |\delta 1|\, (l \cdot (l \cdot \nabla u))l. \tag{A11}$$

Equations (A7) and (A11) imply, respectively, that

$$\frac{1}{|g|}\frac{d|g|}{dt} = -n \cdot (n \cdot \nabla u)$$

$$\frac{1}{|\delta 1|}\frac{d|\delta 1|}{dt} = l \cdot (l \cdot \nabla u)$$

and, since $n \cdot l = 0$, we have $n \cdot (n \cdot \nabla u) = -l \cdot (l \cdot \nabla u)$; therefore,

$$\frac{1}{|g|}\frac{d|g|}{dt} = \frac{1}{|\delta 1|}\frac{d|\delta 1|}{dt} \tag{A12}$$

and, hence, $|g|/|\delta 1|$ is constant along a particle path.

ACKNOWLEDGMENTS

The authors wish to express their appreciation for the anonymous reviewers. The detailed derivation of Eqs. (23) and (25) are taken from O. M. Knio's Ph.D. thesis. The work was supported by the Air Force Office of Scientific Research Grant 84-0356, The National Science Foundation Grant CBT-8709465 and the Department of Energy Grant DE-FG04-87AL44875. Computer support is provided by the John von Neumann National Computer Center.

REFERENCES

1. A. F. Ghoniem, G. Heidarinejad, and A. Krishnan, *In Turbulent Reactive Flow*, edited by R. Borghi and S. N. B. Murthy, Lecture Notes in Engineering, Vol. 40 (Springer-Verlag, New York/Berlin, 1989), 639.
2. A. F. Ghoniem, G. Heidarinejad, and A. Krishnan, *J. Comput. Phys.* **79**, 135 (1988).
3. C. Anderson, *J. Comput. Phys.* **61**, 417 (1985).
4. A. F. Ghoniem and A. Krishnan, in *Proceedings, 22nd Symposium (International) on Combustion* (The Combustion Institute, Pittsburgh, PA, 1988), p. 665.
5. A. F. Ghoniem and A. Krishnan, "Mixing Patterns and the Generation of Vorticity in *A* Density Stratified Shear Layer," Proceedings, Princeton Workshop on Compressible Turbulent Mixing, Lecture Notes in Engineering, in press.
6. A. Krishnan, Ph. D. Thesis, Massachusetts Institute of Technology, 1989 (unpublished).
7. O. M. Knio and A. F. Ghoniem, *J. Comput. Phys.*, in press.
8. G. R. Baker, D. J. Meiron, and S. A. Orzag, *Phys. Fluids* **23**, 1485 (1980).
9. G. Tryggvason, *J. Comput. Phys.* **75**, 253 (1988).
10. R. M. Kerr, *J. Comput. Phys.* **76**, 48 (1988).
11. R. G. Rehm and H. R. Baum, *J. Res. Nat. Bur. Stand.* **83**, 297 (1978).
12. A. Majda and J. A. Sethian, *Combust. Sci. Tech.* **42**, 185 (1985).
13. A. F. Ghoniem, in *Reacting Flows: Combustion and Chemical Reactors*, Lecture Notes in Appl. Math. Vol. 24 (Springer-Verlag, New York/Berlin, 1985), p. 199.
14. A. J. Chorin, *J. Fluid Mech.* **57**, 785 (1973).
15. O. Hald, *SIAM J. Numer. Anal.* **16**, 276 (1979).
16. J. T. Beale and A. Majda, *J. Comput. Phys.* **58**, 188 (1985).
17. J. S. Turner, *Buoyancy Effects in Fluids* (Cambridge Univ. Press, Cambridge, UK, 1973).
18. B. J. Daly, *Phys. Fluids* **10**, 297 (1967).